UNDERSTANDING MEMRISTORS AND SELECTORS FOR FUTURE STORAGE AND COMPUTING APPLICATIONS: MODELING AND ANALYSIS

by

Lu Zhang

Bachelor of Science, University of Science and Technology of China, 2010

Master of Science, University of Pittsburgh, 2012

Submitted to the Graduate Faculty of

Swanson School of Engineering in partial fulfillment

of the requirements for the degree of

Doctor of Philosophy

University of Pittsburgh

2016

UNIVERSITY OF PITTSBURGH

SWANSON SCHOOL OF ENGINEERING

This dissertation was presented

by

Lu Zhang

It was defended on

July 7, 2016

and approved by

Guangyong Li, Ph.D., Associate Professor, Departmental of Electrical and Computer Engineering

Mahmoud El Nokali, Ph.D., Professor, Departmental of Electrical and Computer Engineering

Kevin P Chen, Ph.D., Professor, Departmental of Electrical and Computer Engineering

Qing-Ming Wang, Ph.D., Professor, Departmental of Mechanical Engineering & Materials

Science

Dissertation Director: Yiran Chen, Ph.D., Associate Professor, Departmental of Electrical and

Computer Engineering

UNDERSTANDING MEMRISTORS AND SELECTORS FOR FUTURE STORAGE

AND COMPUTING APPLICATIONS: MODELING AND ANALYSIS

Lu Zhang, PhD

University of Pittsburgh, 2016

The memristor and selector devices are the most promising candidates in the research of emerging memory technologies and neuromorphic computing applications. To understand the device properties and guide for future applications, models for those devices based on physical mechanisms are essential. We developed models for two popular memristors and a selector.

We developed a SPICE-compatible compact model of TiO_2-TiO_{2-x} memristors based on classic ion transportation theory. Our model is shown to simulate important dynamic memristive properties like real-time memristance switching, which are critical in memristor-based analog circuit designs. The model, as well as its analytical approximation, is validated with the experimentally obtained data from real devices. Minor deviations of our model from the measured data are also analyzed and discussed.

We illustrate a heuristic two-state-variable memristor model of charged O vacancy drift resistive switches that includes the effects of internal Joule heating on both the electronic transport and the drift velocity (i.e. switching speed) of vacancies in the switching material. The dynamical state variables correspond to the cross-sectional area of a conducting channel in the device and the gap between the end of the channel and one of the electrodes. The model was calibrated against low voltage pulse-sweep and state-test data collected from a TaO_x memristor so that the contributions of the channel gap, area and temperature to switching can be analyzed.

The model agrees well with experimental results for long switching times and low-to-intermediate voltage operation.

A selector device that demonstrates high nonlinearity, low switching voltage and volatility was fabricated using HfO_x materials with Ag electrodes. The electronic conductance of such volatile selector device was studied under both static and dynamic conditions, with DC and AC measurements respectively. From experimental observations, a compact model is developed in this study to illustrate the physical process of the formation and dissipation of Ag filament for electron transport through the device. A dynamic capacitance model is used to fit the transient current traces under different voltage bias through the device and allow the extraction of parameters associated with the various parasitic components in the device.

TABLE OF CONTENTS

LIST OF TABLES

LIST OF FIGURES

We applied a small reading voltage of 0.2V (10μs) and measured the current to determine the state of the device after each state-evolution pulse. The total time at voltage shown here was 0.101s, and the minimum pulse width was 1us. For each state test, we tuned the memristor to the appropriate initial state for the subsequent ON or OFF switching test. 48

PREFACE

I would like to thank my advisor, Dr. Yiran Chen who led me to the research of memristor and selector modeling. During my PhD study, he provided me with much insightful guidance, and his support helped me overcome the difficulties in the research, and also helped me finish this dissertation. I would like to thank the committee members, Dr. Guangyong Li, Dr. Mahmoud El Nokali, Dr. Kevin P. Chen, and Dr. Qing-Ming Wang, for their help ameliorating this dissertation.

Also I would like to thank Dr. R Stanley Williams, Dr. M-X Zhang, Dr. Zhiyong Li, Dr. Gary Gibson and other researchers in the HP Labs, for their support and guidance in my research of memristor and selector device modeling.

I am very grateful to all the colleagues in EI-lab. It is my pleasure and honor to work with them during the past several years.

At last I would like to thank my family for their encouragement and support. I dedicate this PhD dissertation to my wife, Zelu Wang, who always stands with me and brings happiness to my life every day.

Lu Zhang

Pittsburgh, PA

June 2016

1.0   INTRODUCTION

Researchers are exploring the new candidates for future storage and computing hardware as the demand is growing for large amount of storage, non-volatility (retaining data even when no power supply), high scalability, fast computing speed, as well as reducing power consumption. The research on memristors and selectors brings a huge potential and hope for finding the right candidates. The memristors and selectors can be scaled down to less than 10nm, and provided high switching speed, and high power efficiency. Because of the non-volatility, a memristor can be used in memory and computing technologies to solve the energy and performance problems [25][81][89][90][92][93][97]. And because of the high nonlinearity, a selector can be used (integrated with a memristor) to effectively control the switching access to a memristor, and prevent error in reading/writing of a memristor cell [64].

The special characteristics and advantages that memristors and selectors have intrinsically make them promising for solving the future storage and computing problems in hardware. Both the memristors and selectors are now under wide investigation and research by many researchers and scientists. Numerous experiments are performed to explore new memristor and selector devices, and new switching properties. Besides experiments, researchers are also studying the mechanisms of those devices, and building models to assist their understanding in the devices and guide for research directions. In this dissertation, I have presented my research work in how to understand a memristor and selector from the intrinsic physics and mechanisms,

by building corresponding physical models and mathematical computational analysis. To start, the following section presents a brief history of a memristor concept and selector research.

In 1971 Leon Chua proposed the memristor theory that there should be a fourth circuit element. In his theory the memristor is a circuit element, and its relations with resistor, capacitor and inductor are illustrated [1][2][4]. Afterwards in 2008, HP Labs published a paper announcing that the missing memristor was found and the device was fabricated in lab. The theoretical derivation of the memristor as a fourth circuit element is depicted in **Figure 1** [4]. The memristor concept connects the physical variable flux and electric charge, and the unit is also Ohm, which can be thought as a varying resistor.

A memristor device is a two terminal oxide material device, and it has the resistive switching properties and non-volativity which means it can store the resistance value even when it is disconnected from power and electric source [4]. A memristor's state is determined by the history of voltage and current. The switching is controlled by voltage and the current. Although the realistic memristor device does not directly reflect the relation of flux and charge, it has the nonlinear property and both flux and charge influence the device switching properties.

In most cases, the memristor device has two distinct states. The two different states, i.e. ON and OFF states, can be obtained by applying opposite polarity voltages on the memristor device[4]. The ON and OFF states represent an equilibrium of internal physical and chemical interactions. The control by voltage/current in achieving the ON and OFF states makes memristor devices promising for applications in memory switching cells, as well as for computing hardware cells [15].
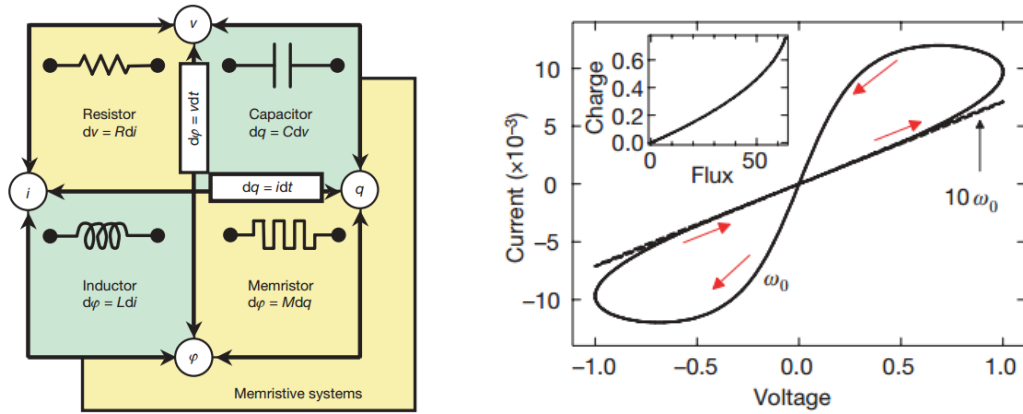
Figure 1. The four fundamental two-terminal circuit elements: resistor, capacitor, inductor and memristor. The memristor describe the relation of charge with flux. The figure on the right shows the ideal IV curve of a memristor, under a sine wave with 1V amplitude[4].

Mathematically, the memristor can be simply described using state variables to illustrate its state dynamics. The equation set below shows the simplest memristor static and dynamic functions [1][2][4]. The variable V is the voltage, variable i is current, w is the state variable which controls the state that a memristor is in. The equation (0a) is the static equation, which tells us about the IV relation of a memristor [4]. The equation (0b) is the dynamic equation for the state change of a memristor [4].

$$V = R(w)i \tag{0a}$$

$$\frac{dw}{dt} = f(w,t) \tag{0b}$$

This set of two equations describes that a memristor's resistance state depends on the state variable w, and the state variable is a time varying variable which is a function. For each

3

fixed state variable w, the relation of voltage V and current i is a linear function. The value of w controls the resistance levels of a memristor, and both ON and OFF states correspond to two distinct values of w.

Experimentally, researchers have demonstrated various types of switching memristive devices, with high switching speed (ns), long retention and endurance, as well as low power consumption. Switching oxide devices, such as TaOx, TiOx, HfOx, etc, have drawn huge attentions from researchers [3][4][5][8][10][18][26][82] [85] [86][87][91][95][96][98][99]. The memristor usually has a switching IV (current and voltage) curve which shows linear or nonlinear switching. The linear switching means that after turning ON, the device remains constant resistance, while vice versa for the nonlinear switching device.

The common IV switching curve of TaOx memristor is shown in Figure 2, from which we can see the linear switching behavior and large ON/OFF ratio [26]. Above 0.5V, the device was turned ON and high current was seen. Afterwards, the decreasing voltage pulses did not change the state of the device until the negative voltages. We can see another turning point in the negative voltage range. The device was ON until that turning point. Beyond the range of -0.6V, the device was turned OFF gradually into high resistance state. Overall this TaO memristor device was robust in switching, with large ON and OFF ratio. The endurance of TaOx memristor is ~10^{10} cycles, seen from the figure below, which is promising for memory cell requirement [26].

4
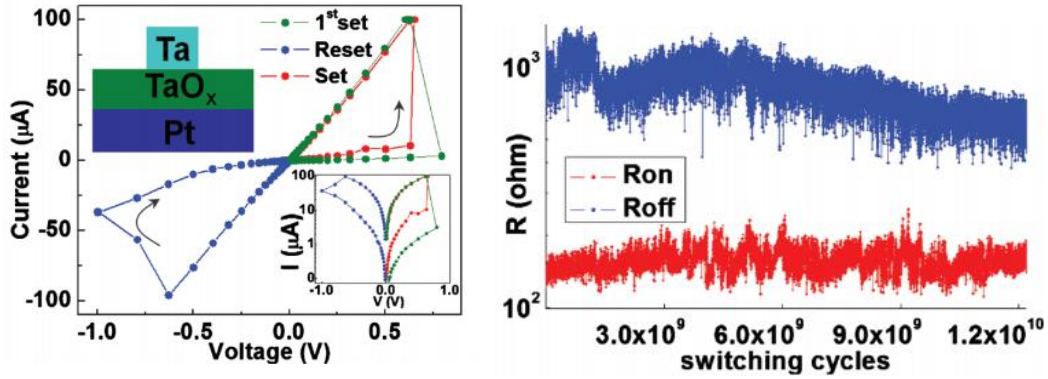
Figure 2. IV switching curve and endurance testing result of a TaOx based memristor. Set/Reset corresponds to turn a memristor to ON/OFF state. The curve is linear switching. The endurance data shows high endurance and ~10 times of ON/OFF ratio[26].

Besides the experiment on a memristor, the model of a memristor is required, in order to quantitatively better understand the device switching and performance behavior, and also to better predict switching properties of a memristor, and guide how to make further improvement in device fabrication. So far, different models for different memristor device systems have been proposed, based on different physical mechanisms. For TiOx and TaOx devices, the filamentary motion has been a major influential factor [6][18][30][82][88][94]. Experimentally, researchers observed both the fast and slow ON or OFF device switching, and that was induced by the filament touching or leaving the metallic boundary of the device electrode region. In addition, the variations are seen in each switching cycle, and that can be explained by the fluctuations of filament tip touching with the electrode region.

Based on the filamentary theories, my modeling work of TiOx and TaOx memristors are derived and built, including both physical equations and experimental data verifications. The two models are also verified by experiment data from HP Labs.

A crossbar, or cross-point structure, is a collection of devices in a matrix structure. A crossbar has multiple input and output ends, and a single device cell connects each input and output. To access a targeted device cell in a crossbar, the corresponding input and output line should be turned "ON" (i.e, input end is connected to electric power source or signal generator, output end is connected to ground). However, there is a significant problem with the reading and writing in a crossbar structure, if no switching control device is implemented or integrated with a device cell. While reading and writing a device cell, the voltage drops can happen on the neighboring device cells, and those voltages can switch or write those devices. Thus a switching control device is essential in a crossbar structure. With this kind of switching control device, only the targeted device cell can be accessed each time, without interference of other untargeted device cells.

A selector device is an ideal solution to solve the sneak current problem. A selector is used to control the switching access to the memristor device in a crossbar structure. The high nonlinearity ensures the sneak current is significantly reduced and also the voltage drop on a memristor is in its operating voltage range. Although different types of selector devices are proposed to be integrated with memristor cells, many of them still lack the requirement for high selectivity and high current density in order to achieve integration of high density memristor-selector cells.

The high nonlinear selector device based on volatile switching conducting bridges developed in HP Labs show promising characteristics with low operating voltages, small device sizes, high selectivity and fast switching speed. The device is the HfO based device, with Ag as filament component after forming.

My modeling work is based on such type of selector device. In the following sections the theory of modeling and data validation are presented.

1.1   DISSERTATION CONTRIBUTIONS

This dissertation solves the modeling research work of TiOx and TaOx memristor devices, as well as the HfOx based selector device. The model of TaOx device is further implemented into Verilog-A model and can be used to run fast circuit simulations. The models can be used for predictions for device switching properties, and also improve understandings of related resistive switching devices.

The contents are listed below.

- TiOx memristor modeling and verification
- TaOx memristor modeling and verification
- HfOx selector modeling and verification, and temperature measurement and analysis of HfOx selector device

1.2   DISSERTATION ORGANIZATION

This dissertation is organized as follows:

Introduction;

Work on TiOx memristor modeling;

Work on TaOx memristor modeling;

High nonlinear HfOx selector device modeling and temperature measurement and analysis of

HfOx selector device.

2.0   BACKGROUND

Research on finding memristor and selector with better switching properties and performance is now increasing. The requirement for high efficiency computing and fast storage is demanding for new non-volatile devices and high nonlinearity selectors. So far researchers have been investigated a wide range of memristor and selector devices. Many of them show promising properties and advantages of replacing the conventional hardware in storage and computing. For memristors, researchers are now exploring smaller sizes, faster speed and longer retention with higher endurance. And for selectors, attention is paid to finding higher nonlinearity and faster speed. In addition, power consumption is also an important factor in those devices. Researchers have demonstrated a variety of memristors and selectors, and showed the differences between those devices (for memristors and selectors), and what advantages they have.

This section illustrates the background research of both memristor and selector devices. Research background about experiment and modeling is presented.

2.1   MEMRISTOR DEVICE RESEARCH BACKGROUND

A variety of memristor devices are researched and demonstrated. The most popular are $TiO_2 - TiO_{2-x}$ memristor, TaO_x memristor, HfO_x and NiO_x resistive switching devices, etc. This section presents the related research work.

The $TiO_2 - TiO_{2-x}$ memristor was first fabricated in HP Labs in 2008 and it was announced as the missing memristor found in the Nature paper by DB Strukov and RS Williams [4]. The modeling research by MD Pickett showed a dynamic switching model of $TiO_2 - TiO_{2-x}$ [18]. This model presented a model with a static IV equation and two equations for the state variable under the ON and OFF switching conditions. The two equations were obtained by regression and fitting parameters.

The TaO_x memristor is one of the most popular memristors in research. According to the paper by J.J Yang in HP Labs, the TaO_x memristor showed high endurance of up to 1×10^{10} switching cycles [26]. That device was a disk device with a diameter of 100 um. Besides the experiment research, TaO_x memristor model by John Paul Strachan in HP Labs showed a one state variable model, with two explicit static and dynamic equations [35]. Although ON and OFF switching were modeled with two separate physical and fitting parameters in the model, and the model was verified with high accuracy by experiment data in the long time transient test. This model presented explicitly the "state variable model" and the dynamic equation of the state variable was obtained by data curve fitting and regression techniques. The temperature and related physical variable dependence were not discussed in this model.

The HfO_x memristor is also popular in research area. The corresponding model by S. Yu presented a trap-assist tunneling physics to understand the mechanisms [10]. In this model, no

state variables were introduced. The transmission rate and probability were calculated explicitly. A set of correlated physical equations were solved in this model.

The NiO_x memristor model by C. Cagli and D. Ielmini focused on solving the set and reset operations by considering underlying physics, with the temperature effects included [46]. Different waveforms were applied to test the device, and the set/reset model were verified by the testing data. No state variables were explicitly presented in this model. Also the set and reset times could be calculated from this model, and failure time under constant voltage stress could be predicted.

The research in other RRAM (resistive random access memory) provides ideas and general understanding into the mechanisms of how the switching can happen. The paper by R. Waser showed the nanoionic mechanisms with the nonlinear drift of ions in set and reset operations, defects and interactions of metal and oxygen atoms, etc [7]. A general picture was presented in this paper on the basic mechanisms of how the resistive switching occurred in those devices.

The memristor devices are still under research and the mystery of the mechanisms is now still being explored and illustrated. My research on modeling the most popular memristors focuses on explaining the main physical mechanisms and providing explicit solutions by considering all necessary equations.

2.2   SELECTOR DEVICE RESEARCH BACKGROUND

A selector controls the switching access to a memristor in a crossbar. The most important property of a selector is the nonlinearity. The research on selectors is mainly on how to improve the nonlinearity while keeping the selectors compactable with memristors in a crossbar. Also there are a wide range of selectors being investigated. This section presents a brief summary of the related selector research work.

One of the most popular selector devices is the NbO_x selector which shows NDR (negative differential resistance) property during the switching. Recently HP researchers proposed a new accurate dynamic model for the electric conduction to explain that the NDR is resulted from a thermal feedback mechanism, in a S-type NDR (voltage-controlled NDR) NbO_x device, as stated in the paper by G. Gibson [64]. The NbO_x selector shows high nonlinearity and fast switching speed. And it is promising in future application of memory crossbar structure. The basic mechanism for this NbO_x selector is caused by the NDR, which is different from the mechanism of HfO_x selector I researched on.

The selector device I have been focusing on is the HfO_x selector, which is based on the volatile conducting bridge, formed inside the device under voltage stress and also dissipates itself when voltage is removed. The conducting bridge, which is formed mainly by metallic atoms from certain layer of a device, controls the switching of a device. The configuration of a conducting bridge determines the resistance state of a device. When the conducting bridge is complete and connects both the top and bottom electrodes of a device, the device is conductive and is in the ON state. Otherwise, when the conducting bridge is not complete, the device is resistive and in OFF state. The volatility is used for the selectivity of such kind of HfO_x selector device. The fast decay of the conducting bridge when no voltage is applied turns the device

"OFF", and blocks the current entering through it. Using that property, the volatile conducting bridge based HfO_x selector is promising as a future selector candidate.

Although we have understood that the basic controlling factor is the conducting bridge in our HfO_x selector device, and there are a variety conducting bridge based memristor devices in research so far, significant differences between those two (conducting bridge based selector and memristor devices) exist.

The CBRAM (conducting bridge random access memory) device is the non-volatile memory device in which a conducting bridge forms inside the device and controls the resistance state [100]. The non-volatility is caused by the fact that, the conducting bridge is relatively strong and large in radius, and also the metallic atoms have relatively low mobility, thus the conducting bridge does not dissipate easily. Both the cross section area and the length of the conducting bridge influence the resistance of the device. In our HfO_x selector device, the decay is caused by the narrowest part of the conducting bridge where atoms have high mobility and can diffuse and also drift under local Coulomb forces.

My modeling research in the HfO_x selector explains why the conducting bridge decay happens, and how it controls the device resistance. In addition, my model gives an explicit expression of the dynamic evolution of device conductance/resistance, from which we can calculate and estimate the device decay time and switching speed.

3.0   MODELING OF $TiO_2 - TiO_{2-x}$ MEMRISTOR DEVICES

The research of memristor devices has attracted overwhelming interests from researchers. While the experimental research on memristor devices has established foundations for higher level memristor device applications, the demand for modeling research and work of memristor devices is still essential. The modeling research can help understand device properties, and can guide the correct research directions. In this section, my research work on $TiO_2 - TiO_{2-x}$ memristor is presented with detailed equation derivations and experiment data verification.

3.1 $TiO_2 - TiO_{2-x}$ MEMRISTOR MODELING INTRODUCTION

The operational characteristics of memristive devices are typically represented by an I-V curve: the memristance of the device changes with the magnitude and pulse duration of the externally applied excitations [4]. As one of the promising technologies, $TiO_2 - TiO_{2-x}$ memristor has recently received significant attention and been widely studied in the solid state device society [3] [7] [32] [34] [42] [43] [44] [45]. Some physical models of memristive devices, such as HfO_x and NiO_x, proposed a general description on the switching on/off procedure based on the ion/vacancy motion driven by the electric field (or potential gradient), which is known as the filament formation or dissolution [8] [9] [39] [46][47] [48] [49] [50]. The behavior of the $TiO_2 - TiO_{2-x}$ device can also be understood by the similar ionic influence: the filament corresponds to the high conductive region while the remaining regions can be treated as low conductive or insulating [3] [7] [30] [51] [52] [53] [54]. Some other models present the understandings on internal state changes under physical factors like electric field and temperature [8][46]**Error! Reference ource not found.**. Some previous work has proposed to model the memristive switching behavior in oxide devices based on the dynamical interactions between electrons, oxygen vacancies, and oxygen anions [55]. However, due to the high computation cost of complex physical quantities, i.e., transition Hamilton matrix and energy density of states, the model cannot be directly applicable to fast circuit simulation. By combining Monte-Carlo method, electron hopping conduction process can be simulated through the similar technique [56]. Kinetic Monte-Carlo method is also implemented to model the filament formation [57]. However, these models do not explicitly give the static and dynamic electrical switching properties of the memristor device. In some TiO_x memristor modeling works, the motion of vacancies is

simulated through classical molecular dynamics [58][59]. The dynamics of tunnel barrier width can be also obtained by modeling the device as a resistor plus Simmons tunnel barrier [18]. In this work, we model the behavior of memristor device from classical macroscopic viewpoint, which is represented by the electron density distribution inside the device. A compact model of $TiO_2 - TiO_{2-x}$ memristor based on classic ion transportation theory is then proposed, targeting the application in SPICE circuit simulations. Compared to the aforementioned TiO_x memristor models, our model offers a concrete calculation of the filament dynamics and derives accurate time-varying behaviors of device resistance changing. Our model, as well as its analytical approximation, well matches the measurements of a real $TiO_2 - TiO_{2-x}$ device on static I-V curve and dynamic pulse programming.

3.2   REGION PARTITIONING AND EQUATION DERIVATIONS
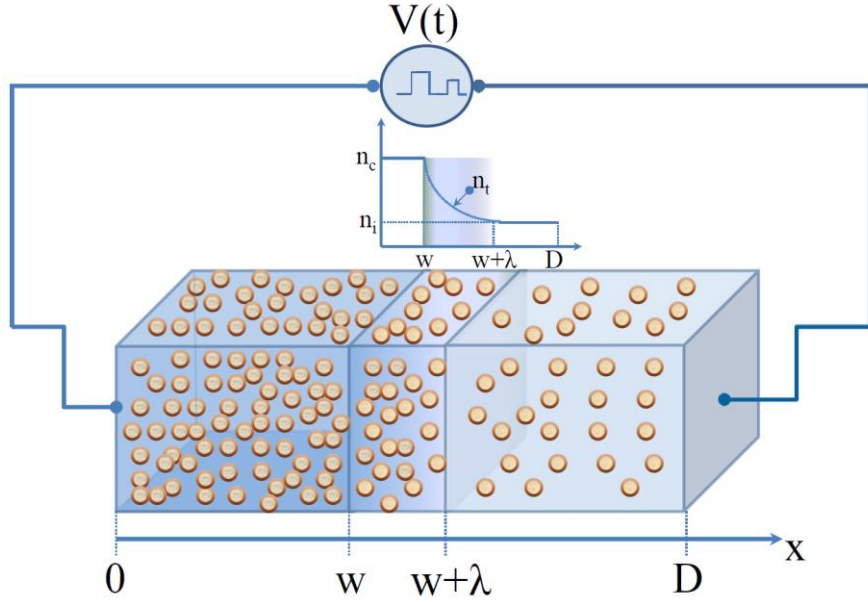
Figure 3. Region partitioning of $TiO_2 - TiO_{2-x}$ memristor.

3.2.1 Region partitioning

We divide a $TiO_2 - TiO_{2-x}$ memristor into three regions, namely, the conductive region, the transition region, and the insulating region, as shown in Figure 3. Here, the conductive region corresponds to the region of filaments while the transition region connects the filaments and the remaining insulating region. The formation or dissolution of the filament is simulated as the ion surface motion within the transition region. We use w, λ, and D to denote the lengths of the conductive region, the transition region, and the entire device, respectively. The real-time current density at position x in the memristor at time t can be expressed as [60]

$$J_s(x,t) = n_s(x,t)q\mu E_s(x,t) - qD_q \frac{dn_s(x,t)}{dx}$$ (1)

Here, the subscript $s = (c, t, i)$ denotes the parameter of conductive region, transition region, and insulating region, respectively. E_s and n_s represent the electric field and the electron density, respectively. μ is the mobility coefficient. q is the elementary charge. D_q is the diffusion constant for electrons. Equation (1) shows that the current is generated mainly from the electron drifting in the electric field and the electron density gradient. D_q is typically small for electron diffusion current, and the second term in Eq. (1) is ignored in our model. If we ignore the variation of the cross section area and assume the current density is uniform in the memristor (i.e., $J_c = J_t = J_i$), the relationships between the electric fields and electron densities of the three regions can be summarized as

$$n_c q\mu E_c(t) = n_t(x,t)q\mu E_t(t) = n_i(t)q\mu E_i(t)$$ (2)

Here, we assume that the E_s and n_s are uniform in conductive and insulating regions and are determined only by the real-time applied voltage (except that n_c is a constant). The equation for the hopping rate of ions in an infinitely large lattice can be expressed as [6] [9]

$$R = fa \sinh(QEa / 2kT)e^{-U/kT}$$ (3)

where R is the ion hopping rate, f is the escape attempt frequency, a is the lattice periodicity, E is the electric field, Q is the charge of ion, U is the activation energy, k is the Boltzmann constant, and T is the local temperature. By considering the fact that the number of generated electrons is proportional to that of the hopping ions inside the thin film, we use the product of a coefficient γ_i and a factor $n_c - n_i(t)$ to approximate the electron density generation function under the influence of electric field in the insulating region. $(n_c - n_i(t))$ also implies that the maximum electron density should not exceed n_c. Hence, the evolution of the electron density in insulating

region under a time-varying electric field E_i can be calculated by the following equation, where γ_i is the electron density generating coefficient in the insulating region in the equation (4) below,

$$\frac{dn_i(t)}{dt} = \gamma_i(n_c - n_i(t))E_i(t) \tag{4}$$

At a given time t and position x, the electric field Et can be viewed as a linear function bounded by E_c and E_i as

$$E_t(x,t) = \frac{E_i(t) - E_c(t)}{\lambda}(x-w) + E_c(t) \tag{5}$$

3.2.2   Derivation of electric field

We note that the voltage $V(t)$ applied on the two ends of the memristor equals the integral of the electric field along the device, or

$$V(t) = E_c(t)w + E_i(t)(D-\lambda-w) + \int_w^{w+\lambda} E_t(x,t)dx \tag{6}$$

Combing Eq. (5) and (6), we have

$$E_c(t) = \frac{V(t)}{w + \frac{1}{2}\lambda + \frac{n_c}{n_i(t)}(D-w-\frac{1}{2}\lambda)} \tag{7}$$

Finally, the transition region length λ reduces when the applied voltage $V(t)$ increases, which is approximated by

$$\lambda = \lambda_0 e^{-|V(t)|} , \tag{8}$$

in our model λ_0 is the transition region length at $V(t) = 0$.

The probability of ion hopping changes with the external electric field. However, the probability is significantly different in the conductive and insulating regions, which leading to the conductivity difference in these two regions. Ideally, every successful ion hopping produces two free electrons and can be viewed as the electron density increase or redistribution. For simplicity, we assume the conductivity in the conductive region (filament) is constant. The motion of ions causes the change of the electron densities in transition and insulating regions, resulting in the formation, growth, and dissolution of the filaments. Since the $TiO_2 - TiO_{2-x}$ device is stable when no voltage bias is applied, we can model the ion motion by considering only the external electric field [6]. The internal temperature of the device, which leads to the fluctuations of cycle-to-cycle switching, is not included in our model. Without loss of generality, we assume the endpoint of the filament starts moving from the left end of the device ($x = 0$) at time 0. $n_t(x; t)$ is the electron density at the position x in the transition region at time t. Compared to the electron density n_c at the boundary between the conductive region and the transition region, the change of the electron density at x is $n_c - n_t(x; t)$, which is mainly due to the oxygen ion vacancy redistribution [5].

3.3 DERIVATION OF FILAMENT AVERAGE MOVING VELOCITY

3.3.1 Derivation of average velocity

When external voltage is applied, the electron densities are changing with time in both transition and insulating regions (filament growth). The electron density increment in an infinitesimal time interval dt equals the difference between the electron densities at positions $x - dx$ and x, or

$$n_t(x-dx,t) - n_t(x,t) = -\frac{dn_t(x,t)}{dx}dx = -\frac{dn_t(x,t)}{dx}v(x,t)dt = \gamma_t(n_c - n_t(x,t))E_t(x,t)dt \qquad (9)$$

Here γ_t is the electron generating coefficient in the transition region. Note that the maximum reachable electron density in the memristor device is n_c, or the region is fully conductive.

Based on Eq. (9), the growth velocity at position x can be calculated by

$$v(x,t) = -\frac{\gamma_t(n_c - n_t(x,t))}{\dfrac{dn_t(x,t)}{dx}}E_t(x,t), \qquad (10)$$

where $\dfrac{dn_t(x,t)}{dx}$ can be derived from Eq. (2) and (5).

The motion of the transition region can be described by the average growth velocity, which is defined as

$$\bar{v}(t) = \frac{\displaystyle\int_w^{w+\lambda} v(x,t)dx}{\lambda}. \qquad (11)$$

This result shows that the filament growth is triggered by mainly the external electric field and can be viewed as the combined imaginary surfaces within the transition region. In the

following sections, we simplify the expressions of n_c, $n_t(x; t)$ and $n_i(t)$ as n_c, n_t, and n_i, which are still the functions of x and/or t.

Substituting Eq. (2) and (5) into Eq. (10), we have

$$v(x,t) = (\frac{n_c}{n_t} - 1)n_c E_c(t) \cdot \frac{\gamma_t}{n_t^2} \frac{\lambda n_c n_i}{n_c - n_i} \tag{12}$$

Substituting Eq. (2), (5), (7) and (12) into (11), the filament growth velocity $\dfrac{dw(t)}{dt}$ can be approximated by

$$\frac{dw(t)}{dt} \approx \bar{v}(t) = \gamma_t \lambda \beta \cdot \frac{1}{\dfrac{n_c}{n_t} - 1} \cdot \frac{V(t)}{w(1 - \dfrac{n_c}{n_t}) + \dfrac{1}{2}\lambda + \dfrac{n_c}{n_t}(D - \dfrac{1}{2}\lambda)} \tag{13}$$

Here β equals $\dfrac{1}{4}\left(\dfrac{n_c}{n_t} - 1\right)^3 + \dfrac{2}{3}\left(\dfrac{n_c}{n_t} - 1\right)^2 + \dfrac{1}{2}\left(\dfrac{n_c}{n_t} - 1\right)$.

3.3.2   Derivation of memristor resistance

The resistance/memristance of the memristor can be calculated by

$$R(t) = \frac{V(t)}{J_c A} = \frac{V(t)}{n_c q \mu E_c(t) A} \;. \tag{14}$$

Here A is the cross section area of the memristor filament. Eq. (13) and (14) describe the dynamic changes of memristor device structure and electrical property, respectively.

3.4 DERIVATION OF MEMRISTOR ON AND OFF SWITCHING TIMES

3.4.1 Derivation of switching time in general case

Assuming n_c and n_i are constant during the switching of the memristor (for example, the applied voltage magnitude is low or the programming pulse width is short), we can obtain the general form of w under a constant applied voltage V by integrating both sides of Eq. (13) as

$$w(t) = \frac{1}{1-\frac{n_c}{n_i}} \cdot \left\{ \sqrt{\left[\left(1-\frac{n_c}{n_i}\right)w(t_0)+C_0\right]^2 - 2\gamma_t\beta\lambda V\Delta t} - C_0 \right\} \tag{15}$$

Here $\Delta t = t - t_0$, $C_0 = \frac{1}{2}\lambda + \frac{n_c}{n_i}(D - \frac{1}{2}\lambda)$. Eq. (15) provides an analytical approximation on the growth of the filaments in the memristor. The internal state variable w is the expression of electron densities and the previous value of w_0. This result bridges two state variables at two different times under one fixed voltage. w represents the filament length, or the state of the device and is able to calculate the state variable value or the total resistance. As we shall see later, this analytical result is close to the experimental result of the total device resistance. Based on that, we can quickly estimate the memristor switching time in the following two scenarios.

3.4.2 Derivation of ON switching time

If the device is switched on, or the filament is formed from the left-end of the memristor to the right-end, at $t_0 = 0$ (or $w(t_0) = 0$), Eq. (15) can be simplified as

$$w(t) = \frac{1}{1 - \frac{n_c}{n_i}} \left\{ \sqrt{C_0^2 - 2\gamma_t \beta \lambda V t} - C_0 \right\} \tag{16}$$

The memristor switching time can be estimated by assuming $C_0^2 - 2\gamma_t \beta \lambda V = 0$, or

$$t_{on} = \frac{C_0^2}{2\gamma_t \beta \lambda V} \tag{17}$$

The corresponding portion of transition region at t0 is $w(t_{on}) \approx D - \frac{1}{2}\lambda$ since $n_i \ll n_c$.

Considering normally $\lambda \ll D$, it indicates that the filament is formed completely at the right end of the memristor at $t = t_{on}$, or the device is totally switched on.

3.4.3 Derivation of OFF switching time

Similarly, if the filament is in the dissolution process starts from the right-end of the memristor at $t_0 = 0$ (or $w(t_0) = D$), Eq. (15) can be simplified as

$$w(t) = \frac{1}{1-\frac{n_c}{n_i}} \left\{ \sqrt{\left[\left(1-\frac{n_c}{n_i}\right)D + C_0 \right]^2 - 2\gamma_t\beta\lambda Vt} - C_0 \right\} \tag{18}$$

The time required to switch off the memristor (t_{off}) can be derived by assuming $w(t_{off}) = 0$, or

$$t_{off} = \frac{\left[\left(1-\frac{n_c}{n_i}\right)D + 2C_0 \right]\left(1-\frac{n_c}{n_i}\right)D}{2\gamma_t\beta\lambda V} \tag{19}$$

3.5   MODEL PARAMETERS AND SIMULATION RESULT VALIDATION

3.5.1   Modeling parameters

Table 1 summarized the three types of the device parameters used in our model, including the geometric parameters, the electrical parameters, and the structural parameters. The electron generating coefficients t and i are derived from the measured data and assumed constant for the different working ranges, as shown in **Figure 4**. We compared our model with the experimentally obtained characterized static I-V curve and dynamic pulse programming curve of a $TiO_2 - TiO_{2-x}$ memristor device.

TABLE I. Modeling Parameters

	Parameters	Value	Parameters	Value
Geometric	D	35nm	A	$0.25\mu m^2$
Electrical	e	$1.602 \times 10^{-19}C$	n_c	$8.75 \times 10^{22}m^{-3}$
Structural	w_0	$0.15D$	λ_0	$0.05D$
Working range		Derived parameters		
$1 \rightarrow 2$		2.3×10^{-6}		1×10^{-6}
$2 \rightarrow 1$		8×10^{-6}		1×10^{-8}
$1 \rightarrow 3$	γ_t	1×10^{-10}	γ_i	1×10^{-9}
$3 \rightarrow 1$		7×10^{-7}		2×10^{-7}

Table 1. Modeling parameters for the $TiO_2 - TiO_{2-x}$ memristor model.

3.5.2   Simulation results of IV and real time resistance evolution
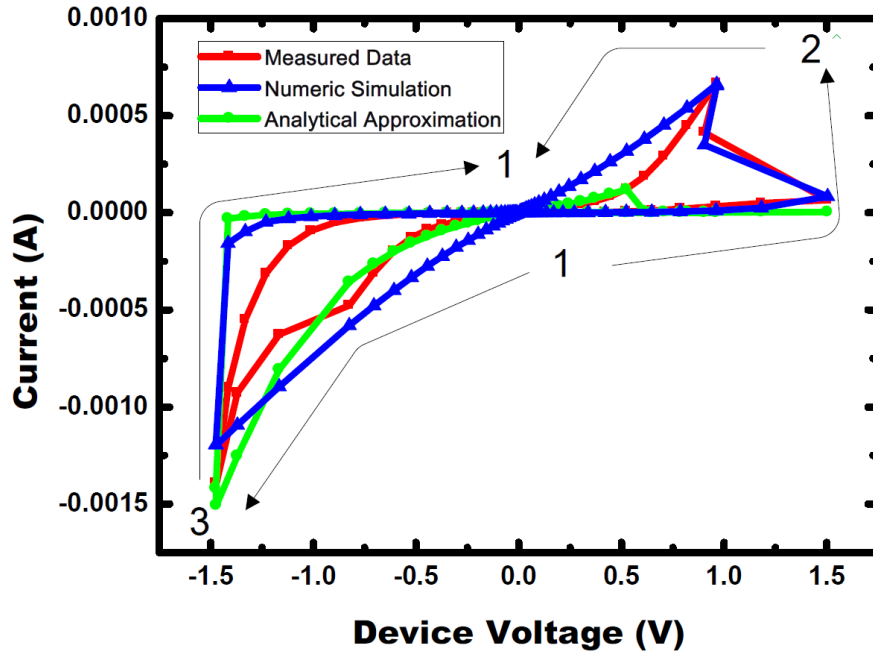
Figure 4. Model validation with static I-V curve, including numerical simulation and analytical approximation. The magnitude of the applied voltage grows exponentially and follows sine function. The memristor is initially set to high resistance state.

Figure 4 shows the measured I-V curve from a real memristor device as well as the experimental data from the numerical simulation and analytical approximation. During the measurement, a sequence of voltage pulses is applied on the memristor device. The magnitude of the voltage pulse grows exponentially, and varies from positive to negative following sine function. The numerical simulation well fit the measured data in all four working ranges. The analytical approximation shows slight discrepancy from the measured data when the resistance is high. It is because the simulated filament growth velocity is lower than the actual value when the variation of ni over time is ignored.

27

To prove the capability of our model on simulating the dynamic switching property of the memristor, we plot the resistance changes following the programming pulses in Figure 5. The resistance of the memristor first decreases when the positive pulses are applied, and then raises when the polarization of the pulses changes to negative. Our numerical simulation matches the measured data very well over most of the plotted points. Small discrepancies show at the high resistance state. One reason for the deviations could be the impact of thermal fluctuations, which become prominent under a relatively low programming voltage. The analytical approximation shows relative large deviation from the measured data at the high-resistance state.
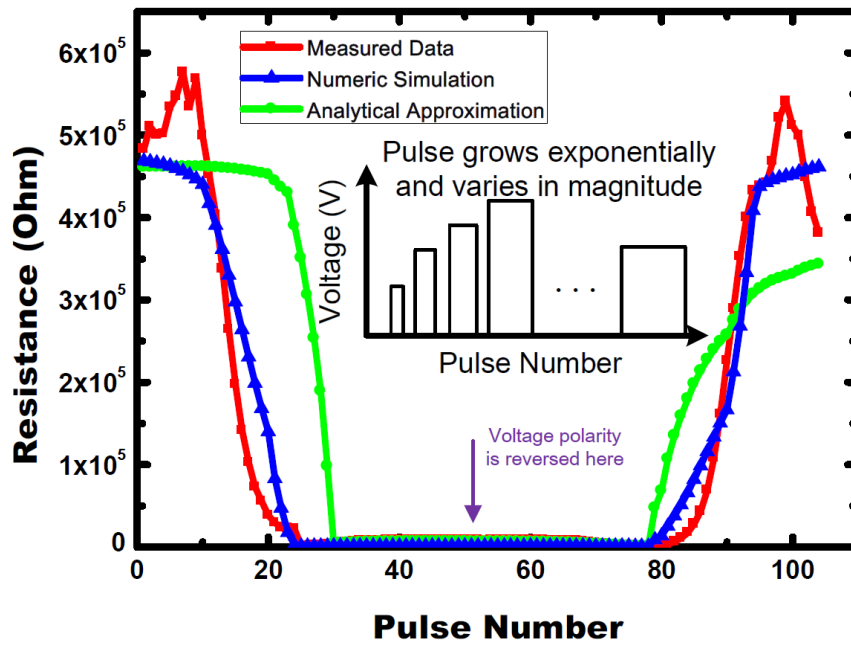
Figure 5. Model validation with memristor dynamic switching for one single cycle, including numerical simulation and analytical approximation.

28

3.6   TIO$_2$ - TIO$_{2\text{-X}}$ MEMRISTOR MODELING WORK SUMMARY

We proposed a compact model to simulate the transition region motion in the $TiO_2 - TiO_{2-x}$ memristor based on the classic ion transportation theory. Our model is validated with the measured data from a real $TiO_2 - TiO_{2-x}$ memristor device and proved capable of simulating the static and dynamic switching properties of the device with high accuracy. This $TiO_2 - TiO_{2-x}$ memristor model also illustrates a novel way to deal with the nonlinear drift, i.e by region partitioning and solving the average velocity of the transition region/filament, from the view of the classic transport physics.

4.0 MODELING OF TaO_x MEMRISTOR DEVICES

TaO_x memristor showed fast switching speed, high endurance and large ON/OFF ratio, from recent experiment research. My modeling work on TaO_x focuses on establishing the direct calculation of current given derived dynamic equations of two state variables. Also the model is verified with experiment testing data. Besides, the model is further implemented into a Verilog-A model for circuit simulations. The Verilog-A model module can be adjusted by changing different device parameters.

The TaO_x memristor model is built based on the two state variables, from which the memristor device state is determined. The two state variables make the model convenient for applications in circuit simulations, compared to the coupled differential equations. Also the model simulated the temperature effects, which is important for realistic device switching test. And my model with the temperature influence included also improves the accuracy for the circuit simulations.

4.1 TaO_x MODELING INTRODUCTION

Research interest in memristors [1][2] has increased dramatically since the demonstration that resistive switching controlled by the drift of charged oxygen vacancies in transition metal oxides is an example of memristive behavior [3][4]. These devices are coupled electro-ionic systems that display strongly nonlinear behavior in both the electronic transport and the charged vacancy/ionic motion [4][5][6][7][8][9][10][11] that controls the conductivity. In order to utilize memristors in circuits, accurate and predictive compact models that can be incorporated into simulators are required. Although the continuity equations for ions, electrons and heat can in principle be solved simultaneously with the Poisson equation to understand resistive switching behavior, such computations require many hours on very large computers, when what is needed are good approximations that will execute in microseconds on a work station. Compact models of resistive switches are best represented by the memristor quasi-static conduction (or state-dependent Ohm's Law) and dynamic state equations of Chua and Kang[2], in which the current-voltage relation depends on one or more state variables that evolve in time when a current is flowing through the device. To date, most such models have utilized only one state variable. However, the fact that transition metal oxides often display two different resistance switching behaviors even in the same device [12], a bipolar mechanism for which ON and OFF switching depends on the polarity of the applied voltage, and a unipolar switching mechanism that is independent of voltage polarity and thus most likely related to Joule heating, is strong evidence that there could be at least two state variables interacting with each other during a switching process [9][13]. We have developed an empirical memristor model using the 'black-box' approach to nonlinear circuit element modeling [14][15] with two state variables and have

31

calibrated it against experimentally measured data from a TaOx device to illustrate the potential of the model for memristor circuit simulations.

Several studies have shown that an oxygen deficient conducting channel is formed inside the switching layer of transition-metal-oxide based memristors, such as TaOx, TiOx, and HfOx [3][5][8][11][16][17][18][19][20][21][22][23][24][25][26][27] [84]. Many experiments have been performed to investigate the switching behavior and mechanisms associated with these channels [3][5][11][16][17][18][19][20][21][22][23][24][25][26][27][84]. Different models have been proposed to explain the experimental behavior [34]. For example, TaOx resistive switches [35][36] have been simulated using memristor models with one state variable that show reasonable agreement with experimental data. In particular, the model of Strachan et al. [35] reproduced fast switching behavior at relatively high voltage amplitudes. The present model based on two state variables is a complementary view in that it accurately describes the behavior under low-to-intermediate voltages (calibrated up to ~0.6V). Kim et al. [37] have proposed a TaO_x model that contains a set of coupled equations and focuses on thermo-electric effects, but such a model is likely too slow to be useful in circuit simulations. Models for other material systems such as HfO_x [8][19][20][38][39] propose field-driven ion migration or electron-trap dynamics as explanations for memristive switching. TiO_x memristor models [17][18] exemplify systems with electron tunneling and nonlinear switching dynamics. Here we present a heuristic two-state-variable memristor model that combines axial drift of charged vacancies in an applied electric field for bipolar switching and radial vacancy motion caused by thermophoresis and diffusion for unipolar switching [13]. This model illustrates the details of the state variable changes during multiple memristor reading cycles, especially the longer term changes that can occur because of thermally-driven unipolar effects.

4.2   MODEL VARIABLES AND EQUATIONS

4.2.1   Model variables

We focus on the dynamical behavior of the geometry of a conducting channel in a transition metal oxide film. Figure 6 shows a schematic figure of the structure, including the insulating film, the top and bottom electrodes, and a conducting channel that nearly but not quite bridges the two electrodes. The channel is defined to be that region in the otherwise insulating film that contains enough O vacancies to have a metallic conductivity [3][4][5][6][16][30]. The channel is approximated here as a cylinder with cross-sectional area A and gap h between the end of the cylinder and the unconnected electrode, which are the two independent state variables in the memristor model. The electron transport mechanism through the gap may be the result of several different tunneling or activated mechanisms either in parallel or a sequential series that depends on the nature of the gap (the value of h) for a particular state [3][16][22].
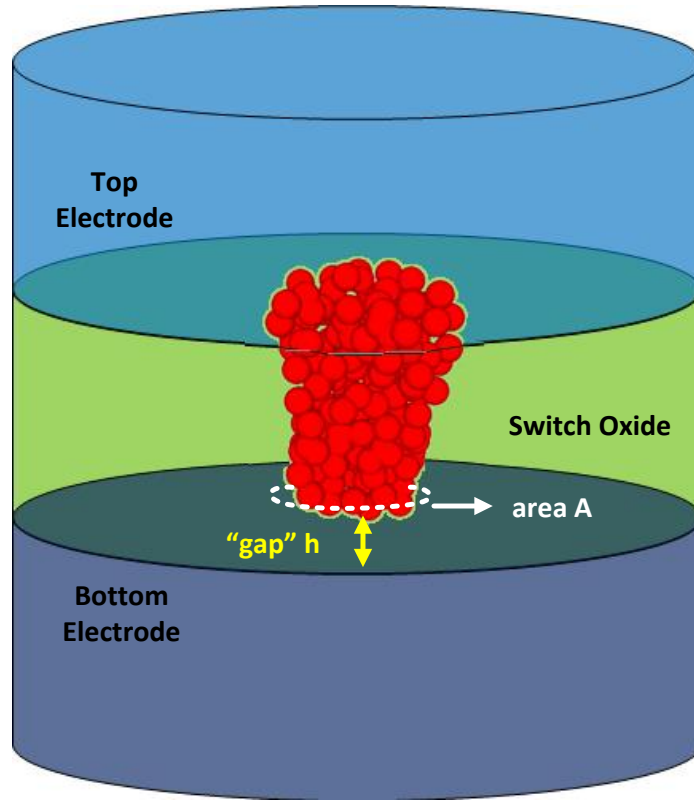
Figure 6. Memristor structure (not to scale) with the switching layer specifically highlighted. The conducting channel is approximated by a cylinder that contains a high enough O vacancy concentration to be nearly metallic. The two dynamical state variables for the system are the channel cross-sectional area A and the gap width h between the end of the channel and the opposing (bottom) electrode.

We chose to use a state-dependent conductance G(h,A) (so our model is actually for a memductor [2]) . We define the variables and parameters as follows: G_1 is the channel conductance; φ is the activation energy for electrons in the gap region; σ_1 is the conductivity of the gap when the barrier height is zero; k is the Boltzmann constant; T_c is the internal local temperature inside the memristor; T_0 is the ambient temperature (assumed to be 300K); e is the electron charge; ε_0 is the vacuum permittivity; and ε_r the stoichiometric oxide relative permittivity. V_0 is a parameter with units of volts that is used in the transition of the conduction mechanism between the tunneling-like states and the ohmic state of the device. The conductance of the wires and other external connections to the memristor is defined as G_s.

4.2.2   Temperature equation

The thermal resistivity of the system γ is the relation between temperature increase and power dissipation in the memristor; the internal temperature of the conducting channel and gap region is assumed to be

$$T_c = T_0 + \gamma I (V - \frac{I}{G_s}) .$$ (20)

4.2.3 Conductance and conductivity equation

The conductance of the channel is:

$$G_1 = \sigma_0 \frac{A}{D-h},$$

<div align="right">(21)</div>

where D is the total width of the oxide film, the variable h is the gap width, and $D - h$ is the length of the conduction channel. The channel conductivity σ_0 varies approximately with the temperature T_c as

$$\sigma_0(T_c) = \sigma_0(T_0) \frac{1}{1 + \beta(T_c - T_0)},$$

<div align="right">(22)</div>

where β is the temperature coefficient of resistivity, $\sigma_0(T_0)$ is the conductivity at ambient temperature, and $\sigma_0(T_c)$ is the conductivity at temperature T_c.

4.2.4 Static IV equation of memristor

Considering the contributions of the external wires, the conducting channel, and the gap conductance, the state-dependent conduction equation is:

$$I = VG,$$

<div align="right">(23a)</div>

$$G = \frac{1}{\left(\dfrac{1}{G_s} + \dfrac{1}{G_1} + \dfrac{h}{\sigma_1 A} \exp(\dfrac{\varphi}{kT_c}) \exp(-\dfrac{e}{kT_c} \sqrt{\dfrac{e}{\pi \varepsilon_r \varepsilon_0} \dfrac{V_0}{h}})\right)}.$$

<div align="right">(23b)</div>

The electronic transport in the gap region is modeled with an empirically modified Poole-Frenkel conduction equation (Frenkel, Oct 1938) [35][40], and the two state variables enter into the expression for the total conductance in a straightforward fashion.

4.3   DYNAMIC EQUATIONS OF TWO STATE VARIABLES

4.3.1 Gap width state variable equation

We also chose the dynamical equations for the two state variables empirically. In the vertical direction (parallel to the axis of the channel), an applied electric field moves the vacancies, causing the end of the conducting channel to extend or contract [4][17]:

$$\frac{\partial h}{\partial t} = v_f = af \sinh\left(\frac{qEa}{2kT_c}\right)\exp\left(\frac{-U_a}{kT_c}\right),$$

(24)

$$E = \begin{cases} \dfrac{V - \dfrac{I}{G_s} - \dfrac{I}{G_1}}{h}, \text{(ON switching)}, \\ \dfrac{I}{G_1(\mathrm{D-h})}, \text{(OFF switching)} \end{cases}$$

(25)

where t is time, v_f is the nonlinear drift velocity of the vacancies, a is the hopping distance, E is the magnitude of the electric field that drives vacancy motion, U_a is the energy barrier between adjacent allowed vacancy sites, and f is the O vacancy jump attempt frequency.

4.3.2 Filament area variable equation

The dynamical equation for the conducting channel area A is approximated by considering the competition between vacancy diffusion and thermophoresis [13]:

$$\frac{\partial A}{\partial t} = \alpha(\frac{I^2}{A} - \Delta),$$

(26)

where α is a parameter that relates power density inside the memristor to the rate of radial vacancy motion and the parameter Δ is the critical power density above which the thermophoretic vacancy flux (which is directed inward toward the center of the channel, since vacancies migrate up a temperature gradient) exceeds diffusion (directed outward, i.e. down the vacancy concentration gradient) and the channel cross section area grows. We can see that, for a fixed total power (or current I), the area will increase until it reaches a steady state value if the initial value of A is small, and vice versa. Similarly, an increase (decrease) of the current will increase (decrease) the value of A. This behavior can lead to a gradual and long term change in the operating characteristics of a device.

4.4 EXPERIMENTS AND MODEL VALIDATION

4.4.1 Experiment device structure

We now have a set of equations to describe the dynamical switching behavior of a memristor based on oxygen vacancy axial drift and radial thermophoresis in a thin metal oxide film.   In order to calibrate our model, we performed both pulse sweeps and state tests to compare our simulation results with experimental data.   We fabricated and measured TaOx memristor disk devices with a diameter of about $100\,\mu m$. All the samples had identical thin film stacks obtained from the same processing run with a stack structure (top to bottom) of Pt 10nm/Ta 30nm/TaOx 11nm/Pt 100nm/Ta 1nm. The broad area bottom Pt electrode preceded by a 1nm Ta adhesion layer was sputter-deposited onto a thick SiO2 film on a Si substrate, and served as a common ground. Subsequently, a blanket 11nm Ta2O5 oxide layer was sputter-deposited onto the bottom electrode at room temperature. Circular 30nm thick Ta electrodes were deposited on top of the oxide through a shadow mask at ambient temperature, followed by 10nm of Pt for a protection layer to prevent oxidation in air and obtain better electrical contacts. The device measurement procedure is shown schematically in Figure 7.
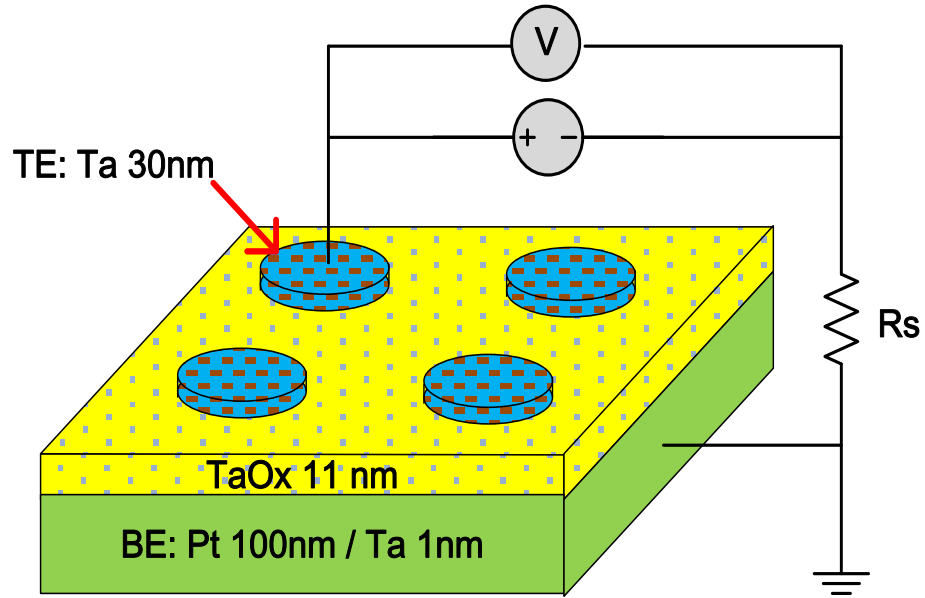
Figure 7. Schematic illustration of the experimental procedure. TaOx memristors were fabricated on a Pt/Ta blanket bottom electrode by depositing an 11 nm TaOx film and 100 micron diameter Ta top electrodes. Two-wire electrical characterization was performed by applying a pulse with a defined voltage and time across an individual device and determining the resulting state by measuring the current through the device at +0.2V.

4.4.2　Pulse sweep test experiment setup

We performed two-probe measurements using the waveform shown schematically in Figure 8 on the memristors to obtain switching curves. The apparatus contains an endurance test board which can also be used to perform pulse sweep test, a current compliance board and a microscope. The endurance board can supply different pulses under different operation modes. The forming was done also using the pulse sweep, in which we control the forming voltage and sweep voltage intervals and pulse width. The memristor device was formed to a steady high conductance state, after which we performed several small voltage read. Then we performed the OFF switching to tune the memristor to low conductance state and began our experiments. The current compliance board can control the current compliance.
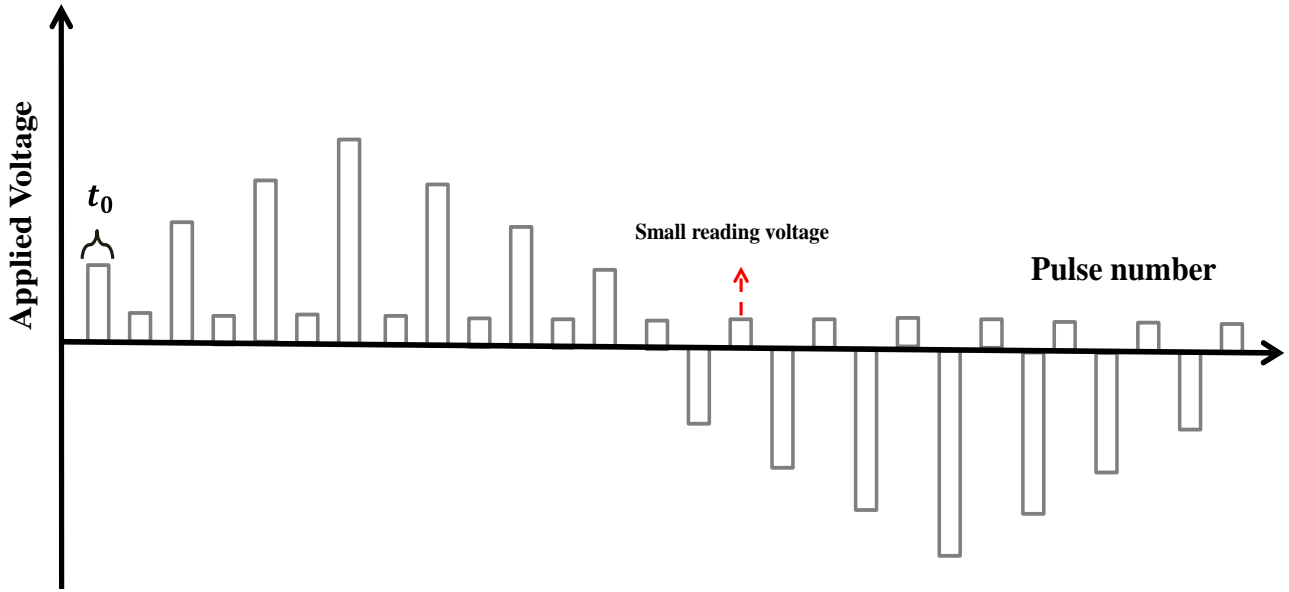
Figure 8. Schematic illustration of the waveform of the pulse sweep test. The device state was changed using a ramped set of 2μs pulses that increased or decreased by 0.01V per subsequent step. After each pulse, a 1μs reading pulse of +0.2V was applied across the device and the current measured to reveal the state of the memristor.

4.4.3 Pulse sweep test simulation IV results validation

In our measurement, we turned the current compliance off in order to observe the full behavior of current during switching. The external series resistance was determined to be 258 ohm in our experiments, which was included in the simulations. The measured and simulated I-V plots are shown in Figure 9**a-b**. Experimentally, we saw that the memristor switched ON at about +0.8V and OFF at about -1.3V, with the corresponding switching current up to the mA level. In our simulations, the switching voltages and pulse widths were the same as those used in the measurements, and the simulated I-V curves agreed well with the experimental data. We also plotted the conductance vs. the applied pulse voltage in Figure 9**c**. The simulation results agreed quantitatively with the experimental data except after the turning point voltage during OFF switching. This discrepancy was mainly due to the stray capacitance of the measurement system (not included in the simulation), which caused the switching voltage to be larger and slower than the isolated memristor considered in the model.

Figure 9(**d**) shows the calculated internal temperature during switching as a function of pulse number over five consecutive switching cycles. The model predicts that the maximum temperature increase for the specific device and operating conditions described here is less than 140K above ambient. The temperature is maximized when the memristor is biased in the ON state, and it is minimized each time the applied voltage is near zero (so the power dissipated in the device is near zero).

To observe the influence of the two state variables during multiple ON/OFF sequences, we plotted the measured conductance vs. pulse voltage results for five consecutive switching cycles in Figure 9(**e**) and the simulated results in Figure 9(**f**). The experimental results were highly reproducible. The model behavior is in excellent quantitative agreement with the experimental

results (except as noted before in the region after the OFF-voltage turning point) [41]. Figure 9(**g**) shows the simulated dynamical behavior of the gap width h, which varied from ~2.0 to ~0 nm (physically reasonable values) as a function of switching from the OFF to the ON state, over the five consecutive switching cycles. The large relative change in the gap width in each cycle was responsible for most of the change in the conductance state of the device during switching, and the fact that the OFF state was nearly the same for each cycle accounts for the reproducibility of the simulated conductance vs. device voltage plots. Figure 9(**h**) shows the channel cross section area A vs. pulse number. The initial area of ~10^4 nm^2 corresponds to a channel diameter of ~110 nm, which is in good agreement with previous observations of the active channel width that forms in a large area TaO$_x$ device [29]. The oscillations in A vs. pulse number have a significant amount of structure, which indicate that the competition between thermophoresis and radial diffusion is active. The variation of the channel area during a single cycle was less than 2%, and the trend of the A state variable was to decrease by ~2% during the initial five ON-OFF cycles. Thus, the thermophoretic variations of the channel area are much slower than the changes in the gap width for the voltages and currents investigated, and the area state variable A is mainly detectable as a long-term systematic change in the conductance state of a device.
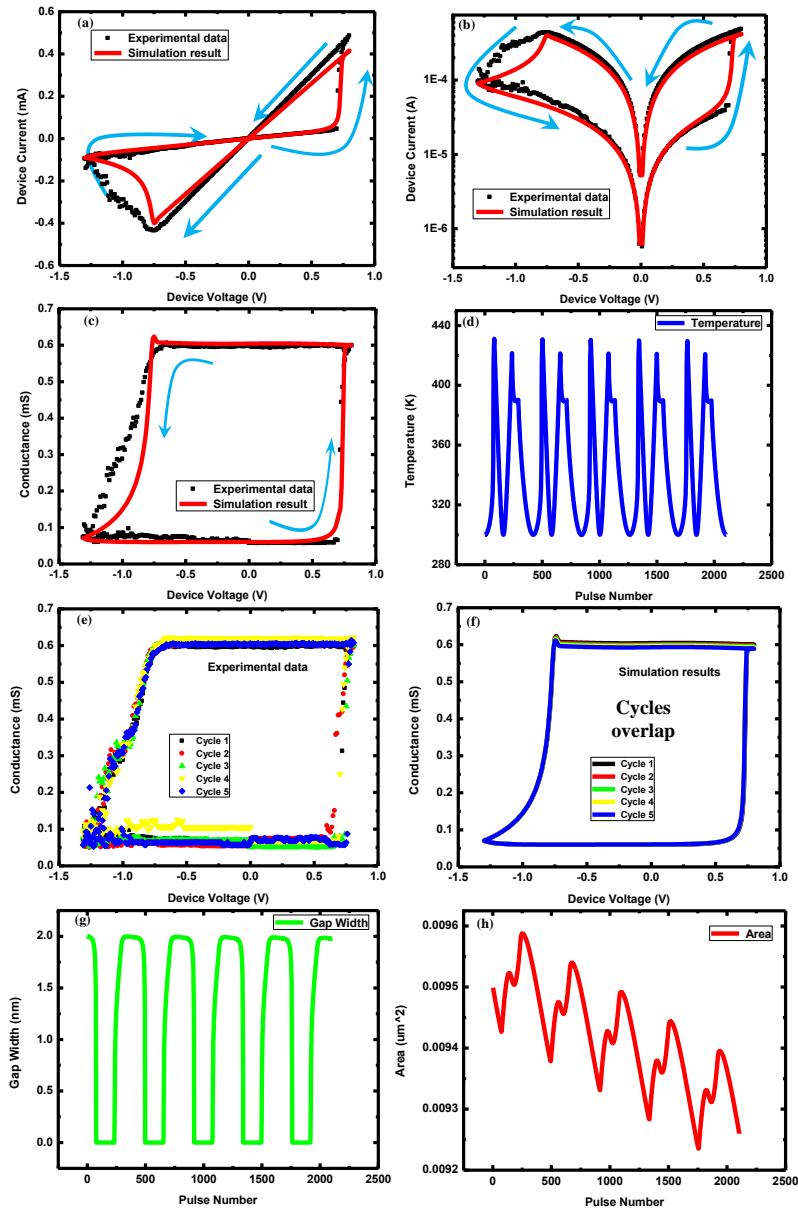
Figure 9. Pulse sweep test measurement results and model simulations. (a) (b) Linear and log scale of the sweep I-V curve: experimental data and simulation result comparisons. (c) Conductance vs. voltage pulse comparison. (d) Simulated temperature vs. pulse number (and thus amplitude). The temperature value was determined for the simulation of the ramped voltage pulses, not the reading pulses. This was done to see the temperature change during the switching process. (e)(f) Experimental and simulated conductance-voltage plots for sequential switching. (g) Gap width h vs. pulse number. (h) Channel cross-sectional area A vs. pulse number. All simulation results except for temperature were obtained at the reading voltage of 0.2V (1μs).

4.4.4 State test experiment setup

To further exercise the model, we performed a state test on the memristor devices with the waveform shown schematically in Figure 10. The experimental setup was different from the previous one, in which we used the Agilent B1530 Parameter Analyer to provide the pulses and control the state test. During the measurement, each pulse with an exponentially growing pulse width is applied on the memristor, after which a single short reading pulse is applied (0.2V, 10μs).
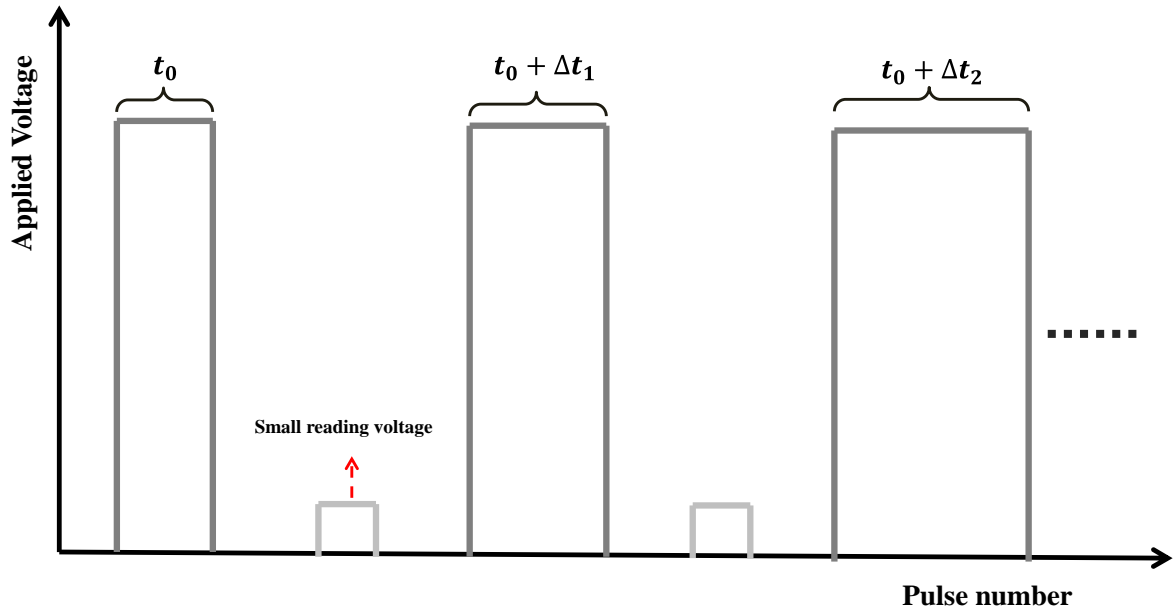
Figure 10. Schematic illustration of the waveform of the state test. The voltage pulses all have the same amplitude, but the pulse width increased exponentially with pulse number. We applied a small reading voltage of 0.2V (10μs) and measured the current to determine the state of the device after each state-evolution pulse. The total time at voltage shown here was 0.101s, and the minimum pulse width was 1us. For each state test, we tuned the memristor to the appropriate initial state for the subsequent ON or OFF switching test.

4.4.5 State test simulation results validation

The experimental and simulation results for times from one microsecond to 0.1 second and a selection of bias voltages are compared in Figure 11. Small voltage amplitudes (e.g., $|V| \leq$ 0.3V) do not change the conductance substantially, showing that the reading voltage did not cause a significant measurement error of the state in the experiments. Interestingly, both voltage polarities for $|V| = 0.3$V caused the conductance of the devices to increase slightly over long times (a unipolar switching effect), even though for the -0.3V case the device was already in a nominally ON high conductance state.   For intermediate voltage amplitudes (e.g. $\pm$0.6V), there are significant conductance changes over a time scale of 0.1 second, with a long induction time for ON switching followed by a fast and limited switching event, and a quick OFF switching followed by a long period of little conductance change. The simulations reproduced the trends in the experimental data quite well.   A notable observation for $\pm$0.6V biases was that OFF switching was about two orders of magnitude faster than ON switching for TaOx devices; this was predicted from the high speed switching studies of Strachan et al. when extrapolated back to the lower voltage amplitude range [35], which also correctly determined the absolute switching ON and OFF times observed in our data.
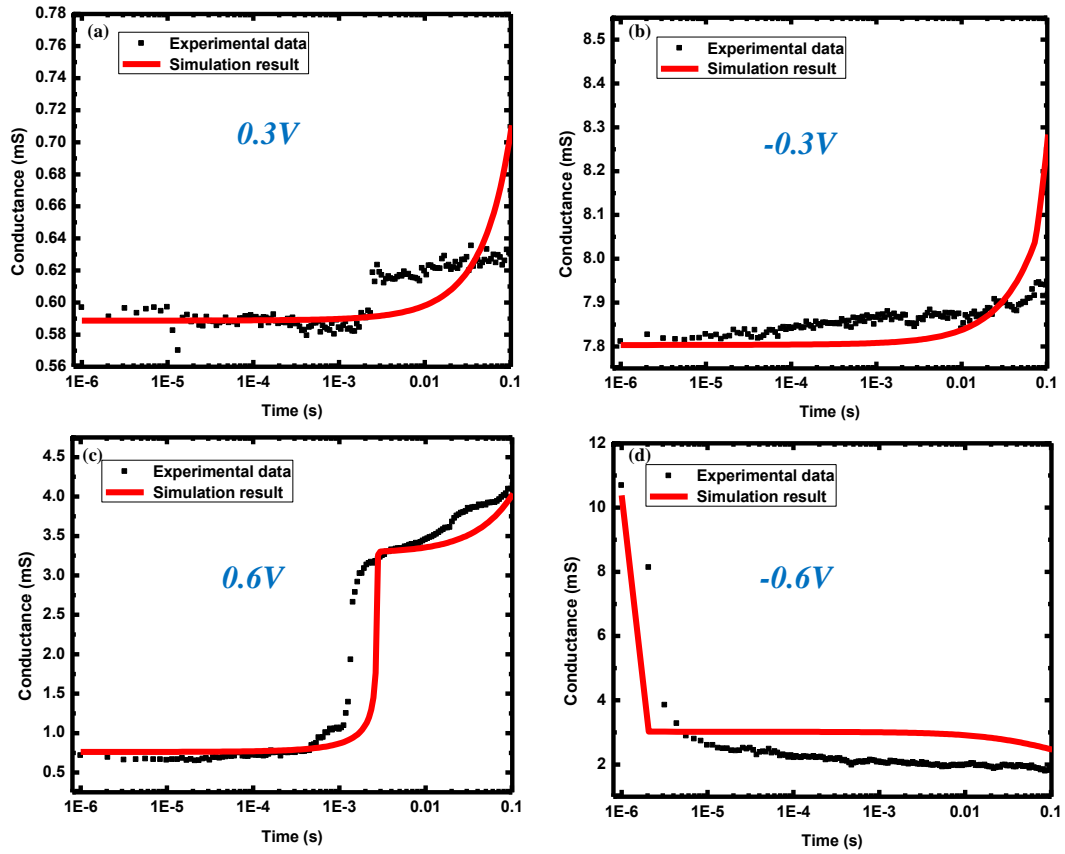
Figure 11. State test results and model simulations. Both positive and negative voltages were applied in the state tests on the same memristor. Small voltages did not change the state of the device significantly. Large voltages switched the device from the OFF/ON to the ON/OFF state. Abrupt changes in conductance vs. time were observed for both experimental data and model simulations. All simulation results were obtained at the reading voltage of 0.2V (10 us).

In Figure 12, we plotted the state variables and internal temperature for memristor switching as a function of time obtained from the simulations for the cases analyzed in Figure 11. In Figure 12**(a)(b),** the small amplitude voltages $|V| \leq 0.3V$ did not cause the gap width to change significantly, which is the reason for the small conductance changes observed in Figure 11. The gap width did change dramatically under intermediate and large biases $|V|=0.6V$, meaning that the memristor successfully switched ON/OFF. This shows that the gap width change dominates the ON/OFF state switching.

Figure 12**(c)(d)** show A as a function time. At low voltages, the changes in A were generally small and required a significant amount of time to accumulate to the point where they could be observed. In Figure 12**(c)**, the reading voltage of +0.2V caused the area A to gradually decrease while a +0.3V bias first minutely reduced the area and then increased it. These observations show that the simulated power density was always below the critical value Δ for the OFF-state device at +0.2V, and thus radial out-diffusion was slightly larger than inward thermophoretic drift in **Eq. 7**. For the +0.3V simulation, the initial simulated power density was still less than Δ, so the area decreased slightly. However, as the conductance of and thus the current through the device increased (because of the change in h), the power density increased and eventually exceeded Δ, after which the channel area increased. For a bias of +0.6V, the power density was always larger than Δ and thus A increased at a slow rate over the entire ON-switching simulation time. In Figure 12**(d),** a small voltage of -0.3V on a device initially in the ON state caused the area A to increase, leading to the unipolar increase in the conductance observed in Figure 11**(b)**. For larger amplitude negative biases (-0.6V), the area decreased gradually over the time of the simulation.

Figure 12**(e)(f)** shows the simulated internal temperature, and the high temperature is seen in ON state under large voltages. However, the area variable has an obvious influence on the conductance and is usually responsible for over switching (too conductive and hard to be turned OFF).
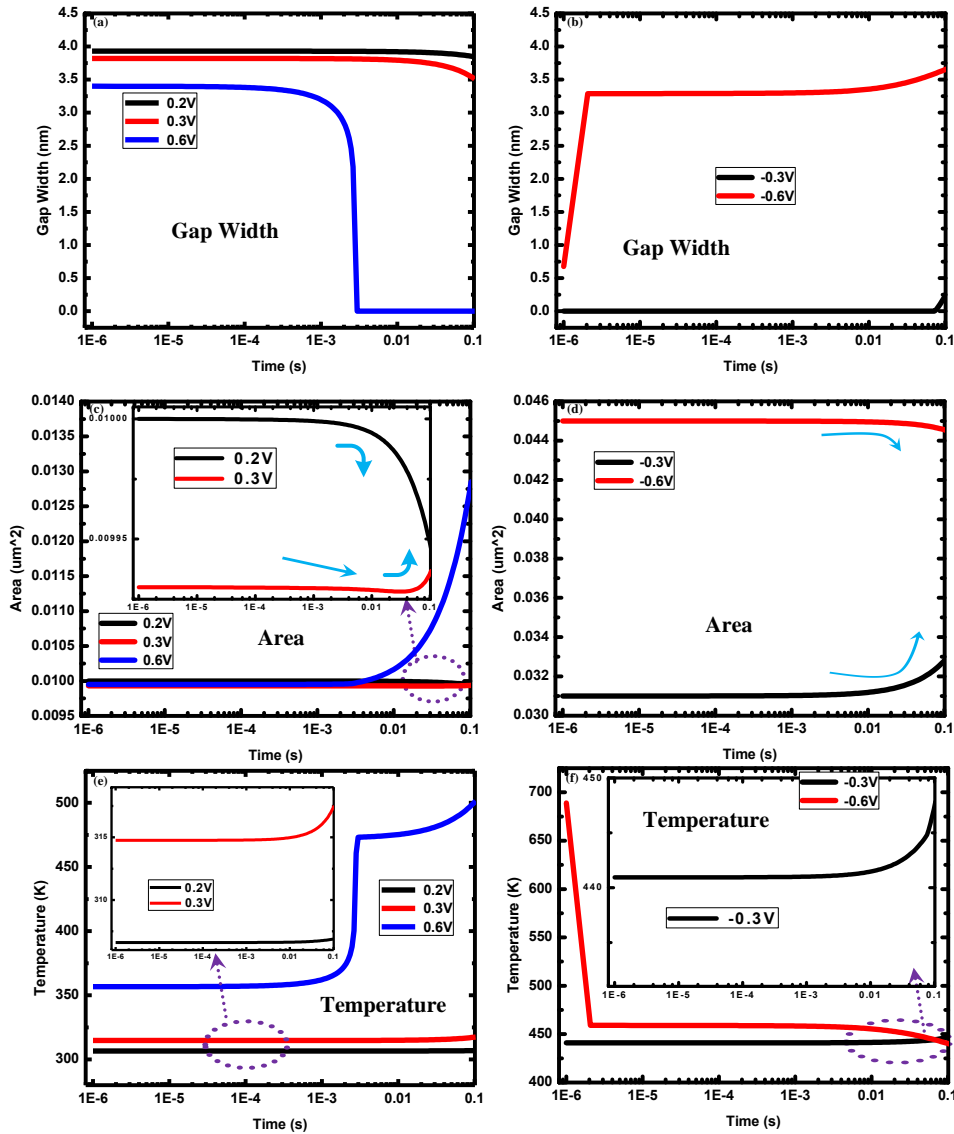
Figure 12. (a)(b) The gap h vs. time. Dramatic changes in h were observed for voltage amplitudes 0.6V. (c)(d) The area A vs. time, for positive/negative state evolution voltages. The +0.3V state test was performed just after the +0.2V test. Thus we applied consistent state variable values for the +0.3V simulation. Areas changed slowly with time. For negative biases, the memristor was reset from the ON state, which was obtained from continuously applying positive voltages. The initial areas should be larger than those for positive voltage state test cases. (e)(f) Temperature vs. time. High temperatures correspond to the ON state with large voltage amplitudes. All simulation results except for temperature were obtained at the reading voltage 0.2V (10μs).

53

4.5   MODEL PARAMETERS

The parameters used in our simulations after the calibrations are in summarized Table 2. There are differences between the parameters used in the pulse sweep and state tests in part because the devices used were different and the process used to form the devices can yield significant differences between devices, and the instruments used to collect the data were different and with such a simple model it is difficult to completely remove the influence of the test system from the model. Thus, when using this model for circuit simulation and design, it is important to calibrate it for memristors in the circuit of interest. As we have seen previously [18][35], we needed different values for some parameters for ON and OFF switching simulations; a more complex/complete model is required to utilize a single set of parameters that is independent of the initial state of the device.

Table 2. Values of physical constants, device constants, and model parameters used in this study.

Physical Constants	ε_0	k	e
Value	8.854E-12	1.381E-23	1.602E-19
Units	F/m	$m^2\ kg/(s^2\ K)$	C

Device Constants	Device Diameter	D	f	a	ε_r	T_0
Value	100	11	1E+13	0.3	20	300
Units	μm^2	nm	Hz	nm		K

Model Parameters		V_0	γ	β	U_a	φ	$\sigma_0(T_0)$	σ_1	α	Δ	R_s
Value	Pulse sweep test simulation	0.1	8E5	0.01	0.62	0.13	8E2	2E1	3E-19	1.2E6	258
	State test simulation		3E5		0.75 (ON) 0.96 (OFF)	0.02	5E3		3E-22	3E6 (ON) 3E7 (OFF)	10
Units		V	K/W	1/K	eV	eV	S	S	m^4/A^2s	A^2/m^2	Ω

4.6 VERILOG-A MODEL OF TaO_x MEMRISTOR

We build the Verilog-A model of TaO_x memristor based on the two state variable model. The Verilog-A model takes the numeric solutions to the differential equations of the two state variables. The model is built into a complete memristor module for circuit simulations. An initial condition and two boundary conditions for two state variables are provided in the Verilog-A model. The model has the following functions:

(1) Given any input voltage waveform V(t), the memristor module can compute the transient current waveform I(t).

(2) The memristor module can adjust the state variables when the boundary conditions are satisfied, thus to make sure the memristor is "functioning" normally.

(3) The parameters of the memristor module can be adjusted according to the simulation requirement for different device parameters.

This model is verified using the same set of parameters as in the two state variable TaO_x memristor model. Same results are obtained (same IV curve). The code is not listed in this dissertation. The figure below **Figure 13** shows a test simulation for the Verilog-A memristor module.
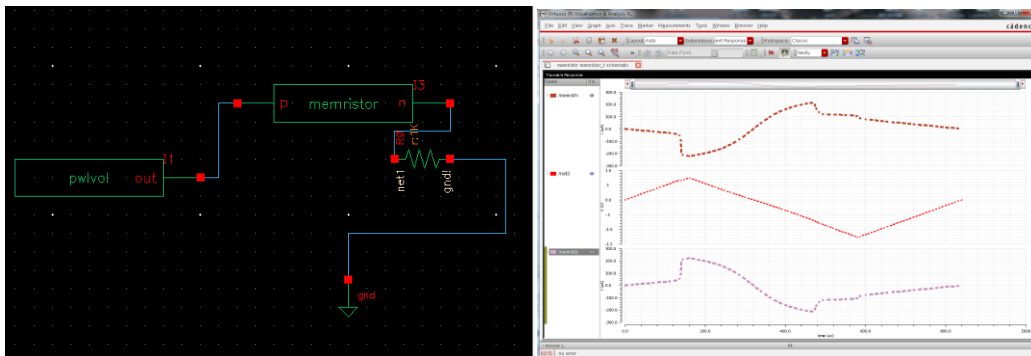
Figure 13. Circuit simulation for the Verilog-A module based on the two state variable memristor model.

4.7 TaO_x MODEL SUMMARY

The two state variables control differently in memristor switching. The gap width represents the electric field contribution to the conduction, while the area reflects the Joule heating effect during switching. The electric contribution makes the memristor to be bipolar switching, and the Joule heating tends to give unipolar switching. Those two aspects compete and determine the final switching state of a memristor.

In summary, we developed a new two-state-variable memristor model and calibrated it with experimental low-to-intermediate voltage amplitude pulse sweep and state test switching data on simple TaOx devices. The model reproduced the experimental data reasonably well over the calibration voltage range. The relatively large test circuit capacitance was responsible for most of the difference observed between simulated and experimental data for the pulse sweep mode. The gap width state variable h was responsible for most of the change of the device conductance within a single switching cycle. The area state variable A was responsible for longer time-scale systematic changes in device conductance over many cycles, and is therefore important in understanding issues such as long term switching stability and endurance. This compact model is suitable for fast circuit simulations (e.g., SPICE-level) because of the simple form of the dynamic equations for the state variables. Further work is needed to incorporate a more physically descriptive model of thermophoresis and to extend the range of validity of the model to higher voltage amplitudes and thus faster switching times.

5.0   MODELING OF SELECTOR DEVICES

A memristor device is promising in memory storage applications. The crossbar structure was invented for such a direct application. Each memristor device represented a storage cell in a crossbar. However, there is a signification problem with the programming of memristor-only crossbar. The sneak current exists which is caused by the voltage drops on neighboring memristor devices, and those voltages actually program those untargeted memristors.

A selector device controls the switching access to a memristor device in a crossbar structure. A selector is in series with a memristor cell in a crossbar, and it can block the sneak current because of its high nonlinearity. A crossbar with both memristor and selector integrated is an ideal candidate for future memory storage architecture.

5.1   RELATED SELECTOR DEVICE RESEARCH

A selector is a switching access device to a memristor in a crossbar structure [1][4][64]. The memrisor devices are in series with selector devices in the crossbar structure [25]. Due to the high nonlinearity, a selector device can block the sneak current and control the switching of the underlying memristor device [62]. Different types of selector devices are studied in the literature, such as NbO2 selector [64][66][67], MIEC (Mixed ionic-electronic conducting) [61], 3D-stackable FAST selector [65][75], punch-through diodes [72], graphene–oxide heterostructures based selector devices [73], varistors which are bi-directional [69], nano-scaled VO2 selector [71], ultrathin metal/amorphous-silicon/metal diodes [75], etc.

The figure below **Figure 14** shows typical switching of high nonlinearity and low voltage bias [76][77]. The fabricated selector device is the field-assisted FAST selector.
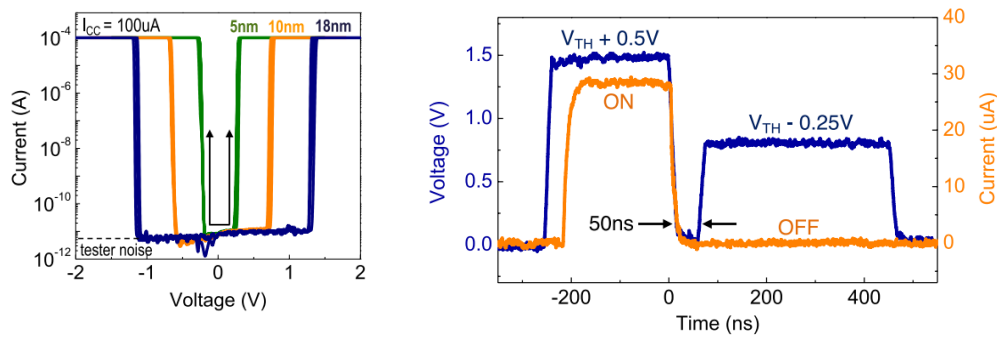
Figure 14. Typical IV curve of the FAST selector and state test using constant peak voltage after which opposite polarity voltage is applied. Fast switching speed of 50ns is observed. Sharp jump of current is observed in the experiment.

The fast switching speed measured shown in the figure above shows promising characteristics for the high selectivity of a selector. With low switching voltages which are in the

comparable range of memristor switching voltages, the device is an excellent candidate for future integration with memristor as a 1S1R cell.

The testing experiments done in HP show similar switching behaviors as those above. The data below shows in **Figure 15** low switching voltages, and low current level, as well as super high nonlinearity.
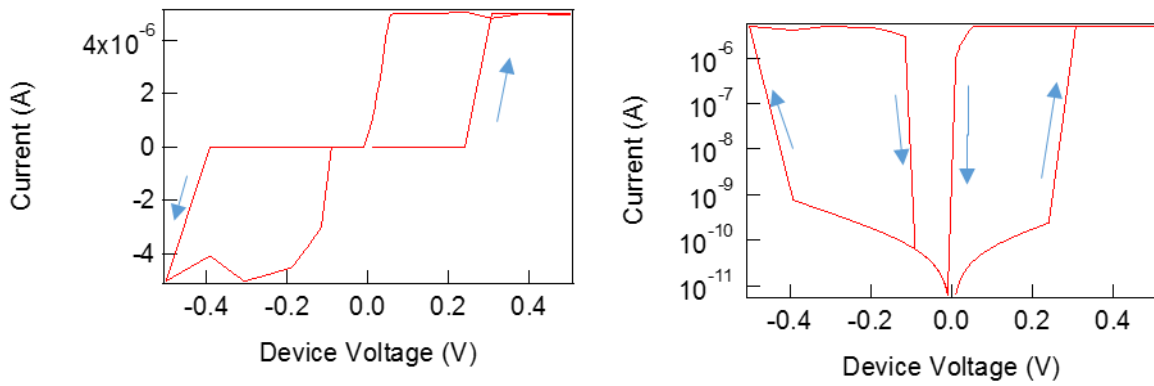
Figure 15. Experiment data measured on a oxide selector in HP Labs. Low voltage at about 0.4V can switch the device, and almost symmetric switching window is observed. 5 orders of magnitude in ON/OFF ratio is tested in the switching curve.

5.2   SELECTOR DEVICE SWITCHING CHARACTERISTICS

A selector device has both ON and OFF switching, which is similar to that of a memristor. In ON switching, the atoms become ionized near the top electrode, and then drift under strong electric field. This process is similar to that of memristor turning ON. The moving ions drift and accumulate themselves at the other end, and finally build up the filament, which is conducting. In this way the conductance increases and ON state is reached. In OFF switching, the atoms near the end of the filament are easily ionized and diffuse, in low or without electric field. The mechanisms are more complex and several factors are analyzed separately for each corresponding model in the following sections.

5.2.1 ON switching model

The ON switching of metal oxide selector device shows similar behavior to that of TaOx memristor device. The sharp jump of IV curve occurred at lower voltage in DC pulse sweep test supposes that there exists a gap which controls the ON/OFF states of selector device. The model focuses on the motion of gap width varying with time under electric field. The equations of memristor state variable dynamics can be directly applied here to describe the nonlinear motion of filament tip, e.g gap width dynamics.

$$\frac{\partial h}{\partial t} = v_f = af\sinh\left(\frac{qEa}{2kT_c}\right)\exp\left(\frac{-U_a}{kT_c}\right),$$ (27)

$$\frac{\partial A}{\partial t} = \alpha(\frac{I^2}{A} - \Delta)$$ (28)

The electric field in equation (27) should always be the field in ON switching condition:

$$E = \frac{V - \dfrac{I}{G_s} - \dfrac{I}{G_1}}{h}$$ (29)

5.2.2 OFF switching model

The OFF switching mechanisms are complicated, in which several parallel physical factors exist and influence the overall property. Observed from experimental data, the main physical mechanisms considered in the model are ionic diffusion, ion drift motion, and thermal effects inside oxide and ionization inside oxide. Models are developed based on individual mechanisms. Below are the specific models with focus on corresponding properties.

5.3   THEORETICAL MODEL 1: DIFFUSION MODEL

The diffusion model describe the ions/vacancies diffuse away in OFF switching procedure. In this model, we introduce the critical boundary and critical density which model sudden change of OFF switching process. The filament inside the oxide is viewed as a density varying cylinder. The conductivity is a function of radius r and density inside the filament. Because the density function is derived as a function of radius r, and we view the mobility μ as constant for simplification, then the conductivity is simplified as a one variable function, of radius r only.

$$\sigma(r, n) = f(n)q\mu(r) \tag{30}$$

$$n(r) = g(r, t) \tag{31}$$

The two equations above include two unknown functions f(n) and g(r, t) in our model. To obtain the explicit form from derivations, we implemented a two-stage approximation for the conductivity dependence on density f(n): simplest step function approximation, and a more realistic smooth function approximation. The function g(r, t) can be derived from solving diffusion equations in cylindrical coordinates. The diffusion and flux continuity equations are:

$$\vec{J} = -D\nabla n(r) \tag{32}$$

$$\nabla \bullet \vec{J} + \frac{\partial n}{\partial t} = 0 \tag{33}$$

Assuming initial ion/vacancy density is uniformly distributed within the cylinder with density u, the diffusivity D, total radius a, and height is h, then we can obtain the density function g(r, t) as follows:

$$n(r,t) = g(r,t) = \frac{u}{2Dt} \int_0^a r' e^{-\frac{(r-r')^2}{4Dt}} \, dr' \tag{34}$$

Thus the overall conductance is calculated from integral of area dS

$$G(r) = \int dG = \int f(n) q\mu \frac{dS}{h} \tag{35}$$

The expression of conductivity dependence on density n function f(n) is chosen as the following as a straightforward step function of critical density nc,

$$f(n) = \begin{cases} n_H, n \geq n_c \\ n_L, n < n_c \end{cases} \tag{36}$$

To make more realistic model, we can choose other smooth functions with critical density nc as an intermediate variable to control the shape of the functions.

Those two important model concepts of critical density and critical boundary are plotted in the figure below **Figure 16**.

In **Figure 17**, the simulation results show the evolution of density profile in radial direction at any given time t, and the total conductance change. The modeling parameters are in the **Table 3**.
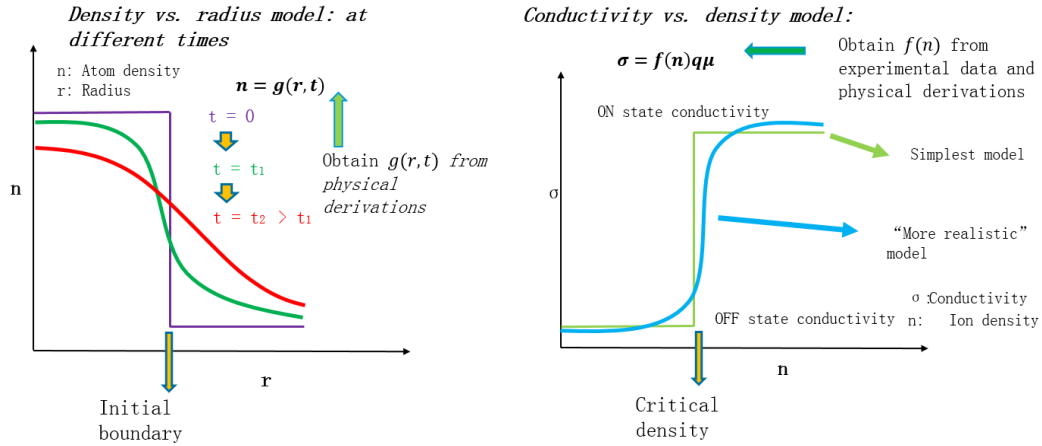
Figure 16. Diffusion model important concepts and pictures. Initial boundary indicates the initial conductance of the selector. Critical density indicates a transition of conductance. Step function and more realistic function are used to simulate the conductance transition of the selector device.

Table 3. Parameters for diffusion model. Conductance decreases to significant small value in ~10us using parameters in the table, which is within experiment observation range.

Important physical parameters	Initial radius r	Bridge tip height h	Initial atom density n	Electron mobility μ	Diffusivity D	Critical density nc	Temperature T
Values	$2\ nm$	$2\ nm$	1e29	1e-6 $m^2/(Vs)$	1e-11 m^2/s	5e28	300K
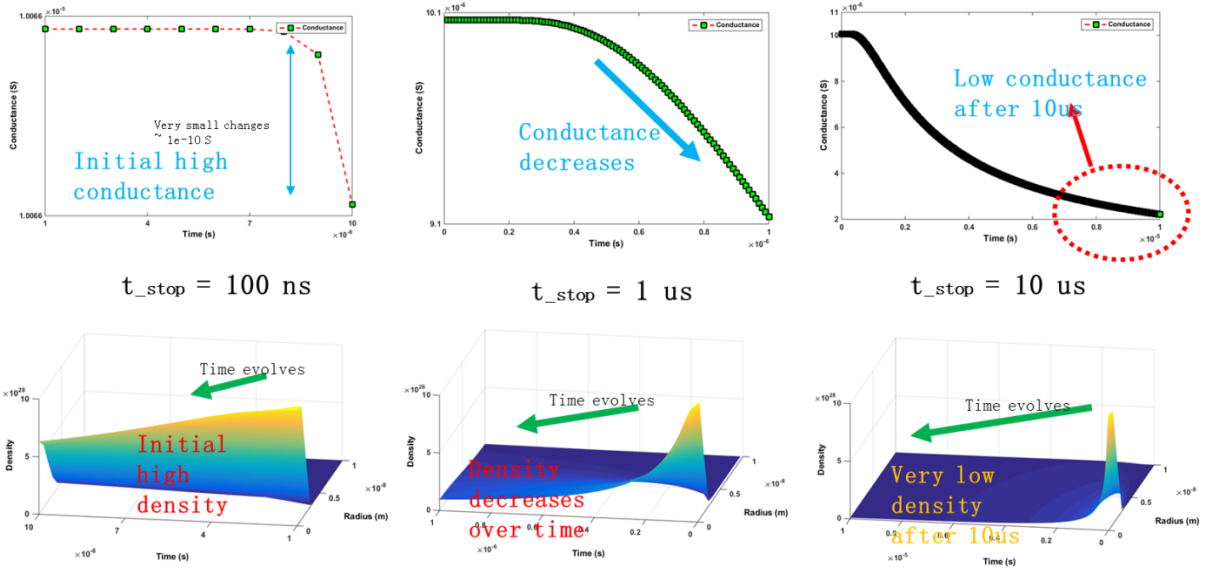
Figure 17. Modeling results using diffusion model. Conductance decreases over time and significant amount of decreasing is obtained at ~10us. Ion density profile is changing over time and also in space. Initial density is accumulated in the center, while after 1us and 10us, density drops to low value at the original center point.

5.4   THEORETICAL MODEL 2: IONIZATION MODEL

The ionization model focus on the mechanism that the atom can be ionized inside the oxide, and then diffuse away or drift under local electric field. Those atoms are especially within the filament tip region. According to the Arrhenius Law, the activated atom rate is given by the equation below:

$$\alpha = \alpha_0 e^{-\frac{E_r}{kT}} \qquad (37)$$

where α is the rate, and Er is the activation energy, T is temperature, k is Boltzmann constant.

In any infinitesimal time interval dt, the ionized atom number is

$$dN = \alpha dt \cdot 2\pi a(t)S_0 \qquad (38)$$

where a is the initial radius, S_0 is the surface atom density in the filament.

The charge of ionized atoms is equal to

$$dq = qdN \qquad (39)$$

Next consider the electric field E on the surface or close to the filament, we can obtain the form of

$$E = \frac{\sigma_0}{\varepsilon_r \varepsilon_0} \qquad (40)$$

σ_0 is the surface charge density, ε_r is the relative permittivity, and ε_0 is the vacuum permittivity.

In the space while ions are drifting, the time interval for moving dz distance is equal to

$$dt = \frac{dz}{\mu E} \qquad (41)$$

By combination of equation (40) and (41), we derive the equations for change of charge density $d\sigma_0(t)$, and electric field dE(t), in any infinitesimal time interval dt.

$$d\sigma_0(t) = \frac{dq(t)}{A} \tag{42}$$

$$dE(t) \approx \frac{d\sigma_0(t)}{\varepsilon_r \varepsilon_0} \tag{43}$$

The variable A is the area of the filament surface where charge amount q exists. If we view the stream of moving ions in the space as steady and continuous, we can define the space linear density γ indicating the number of ions per unit distance in space. Thus the ion number in the stream in time interval dt is obtained by

$$dN = \gamma |dz| \tag{44}$$

$$d\vec{z} = \vec{v}dt \tag{45}$$

$$\vec{v} = \mu\vec{E} \tag{46}$$

By combination of equations (38) - (46), we can obtain the electric field as a function of time t, given the initial electric field magnitude E0 at time t=0.

$$\vec{E} \simeq \vec{E}_0 \exp(-\frac{q\gamma\mu}{\varepsilon_r \varepsilon_0 A}t) \tag{47}$$

$$a(t) \simeq -\frac{\gamma\mu}{2\pi S_0 \alpha} E_0 \exp(-\frac{q\gamma\mu}{\varepsilon_r \varepsilon_0 A}t) \tag{48}$$

The total conductance is calculated from equation (35) with integral of radius a(t) and with assumed constant conductivity,

$$G(t) = \int dG = \int \sigma_c \frac{2\pi a(t) da(t)}{h} \tag{49}$$

$$G(t) = G_0 \exp(-\frac{2q\gamma\mu}{\varepsilon_r \varepsilon_0 A}t) \tag{50}$$

68

The parameters for the model is summarized in the Table 4, and are reasonable according to experimental observations and data.

Table 4. Parameters of ionization model. All parameters are reasonable from experiments. Calculated decreasing time is about 10us using parameters in the table.

Ionization model parameters	q	γ	μ	ε_0	ε_r	A
Values	3.2e-19 C	$1\ nm^{-1}$	$0.001\ \mu$m $^2V^{-1}s^{-1}$	8.85e-12 Fm^{-1}	4	$10\ nm^2$

The simulated conductance decrease is an exponential function, and more details are discussed in the following sections.

5.5 VOLATILE CONDUCTING BRIDGE BASED SELECTORS MODELING

5.5.1 Introduction

The memristor was proposed by Leon Chua as the fourth circuit element in 1970s [1][2]. The fabricated memristor device was launched in HP Labs in 2008 [4]. This kind of memristive device has special properties of non-volatility, as well as faster switching speed, long endurance and retention. The memristor devices are promising in memory storage and neuromorphic computing hardware applications [15][25]. A variety of memristor devices have been studied. Popular memristive devices are mostly metal oxide based devices with adjustment of oxygen and metal content, such as TiOx, TaOx, HfOx devices [3] [4] [6] [7] [17] [18] [26] [35] **Error! eference source not found.** [74] [78]. The switching of those memristive devices results in two distinct states, ie. ON and OFF state, which corresponds to high and low conductance respectively. The binary states of memristor devices can be used for the new memory technologies. For the application in high density memory, a memristor device is integrated in a crossbar architecture [79]. However, there is a significant problem with the memristor-only crossbar programming, which is caused by the sneak current. The sneak current exists in the crossbar structure, which is caused by noisy current through neighboring memristor cells, and that noisy current also flows through the memristor cell under programming. In this case, a switch control device is essential in a crossbar to ensure that any other neighboring memristor cells are not programmed while programming a target memristor cell. And a selector device is an ideal solution to this problem.

A selector is a switching device that provides access to a memristor in a crossbar structure [1][2][4][64]. The memristor devices are in series with selector devices in memory cells at the intersections of the addressing lines in the crossbar structure [25]. Due to their high nonlinearity, selectors can block undesirable leakage currents through unselected memory cells in a crossbar array, enabling one to address only a single selected cell [62]. Different types of selectors are reported in the literature, such as NbO2 selectors [64][66][67], Mixed ionic-electronic conducting (MIEC) selectors [61], 3D-stackable FAST selectors [65][75], punch-through diodes [72], graphene–oxide heterostructure based selectors [73], varistors that are bi-directional [69], nano-scaled VO2 selectors [71], ultrathin metal/amorphous-silicon/metal diodes [75], etc.

we fabricated a new volatile selector device based on a HfOx solid electrolyte with silver electrodes in a micron scale crossbar structure, and studied the device switching and conductance decay properties extensively. A compact model was built to explain quantitatively how the conducting filament formed and dissipated in the device. Our model was derived from intrinsic physical processes, and was implemented as an individual module, which could be further applied to 1S1R (1 selector in series with 1 resistor, which can be a memory element such as a memristor) cell simulations. Compared to other selector models reported in the literature to date, this new model demonstrates a good fit for the relaxation speed and selectivity observed in the devices.

71

5.5.2 Experiment process and device fabrication details

The structure of our selector device was Pt/HfOx/Ag/Pt. The selector devices are micron size crossbar, with Ta 2nm/Pt 15 nm as BE (bottom electrode) evaporated through shadow mask. Ta 2nm was used as an adhesion layer between Pt BE and Si substrate covered with 200nm thermal SiO2. A blanket 15 nm HfOx film is sputtered form HfO2 oxide target, assisted with O2 flow during deposition to prevent oxygen vacancies in HfOx. Top electrode (TE) consisted of 5 nm Ag.20nm Pt deposited through shadow mask, with Pt as the capping layer over Ag as well as the probing contact.

5.5.3 Modeling figure illustrations

The switching characteristic was mainly controlled by the conducting bridge (CB) formed by Ag atom clusters. The selector device was formed by the initial high positive/negative voltage (about ±1.8V under the transient test, almost symmetric), and then the CB of Ag atom clusters was built. The current compliance was removed in this transient test condition. In **Figure 18**, the Ag atoms near top electrode became ionized and moved toward the bottom electrode. When the ions reached the CB edge, they accumulated and became neutralized Ag atoms again by the excess electrons near the CB body and bottom electrode. In this way a complete CB was formed. Due to localization and surface tension [63], the CB might be non-uniform in cross section area inside the device, and there were weak and thin segments of CB which consisted of a few atoms. In our model, such a weak segment was called "CB tip" and it was considered to bridge between the end of the larger CB body and the top electrode. The CB consisted of discontinuous Ag clusters. The conduction was mainly via electron tunneling in this condition, and the selector device resistance was relatively high, about a mega-ohm in the ON state. To stabilize the CB, a holding voltage was required to maintain the CB tip structure and keep the device in the ON state. When the voltage dropped below the holding voltage, the CB tip decayed and the device conductance decreased. The formation of an "end to end" CB put the device in a higher conductance state (still mega-ohm but more than 30 orders high in conductance magnitude), which was similar to the ON switching of a memristor device, during which the filament was formed from end to end and the device was conductive [3] [6] [7] [18] [17] [35] [74] [80]. Compared to the non-volatile CBRAM memristor device whose switching is also controlled by the CB filament [68], our device shows volatility. The rupture of the CB is not common in most

memristor and selector devices [3], and it is this property that might contribute to the volatile switching of our selector device.

According to our model, the decay of the CB occurs near a weak spot in the bridge where its radius is minimum, which for the sake of illustration we take to be near the end of the bridge as depicted in **Figure 18**. And that weak spot in the bridge is called a CB tip in our model, the radius of which is much smaller than that of a CB body in our model. The Ag atoms and ions have relatively high mobility in oxides [70]. In **Figure 18**, the bridge tip consists of small number of atoms, and some atoms can be ionized and move away more quickly due to the mutual Coulomb repulsion caused by ion charges within the CB tip. Thus in our model for the decay of the CB, both atomic and ionic diffusion and drift are considered as causes for decrease of CB tip radius. The thermalization time for our structure is faster than its experimentally measured conductance decay time. The time scale for thermal diffusivity is on the order of nanoseconds while the observed electrical conductance decay occurs in microseconds. Thus, thermophoretic forces on the atoms as a decay mechanism for the conductive bridge are not discussed in this model [13][80].
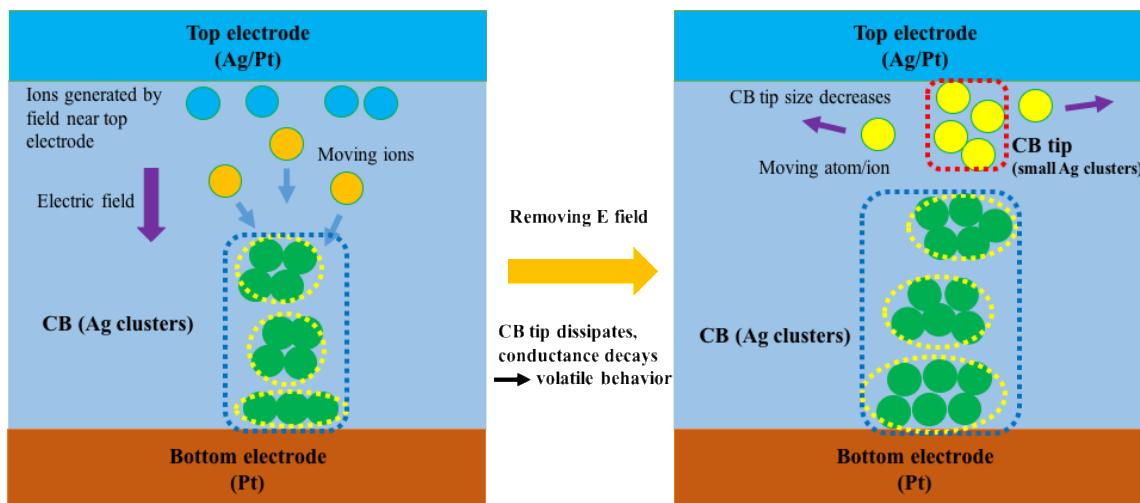
Figure 18. Illustration of our selector device switching mechanisms. The formation of CB under electric field is shown in the left figure. The decay of conductance and CB when the electric field is removed is shown in the right figure. Ag atoms/ions in the CB tip have high mobility and the dissipation of Ag atoms/ions causes the rupture of the CB. The CB consists of discontinuous Ag clusters in our case, and CB tip consists of countable Ag atoms, which is relatively small compared to the CB structure.

5.5.4 Model derivations: dynamic resistance model

In our model, the electrically switching portion of the CB is a narrow cylinder with an initial radius r_0 as shown in **Figure 19**. Inside this narrow cylinder, there are very small number of Ag atoms and ions. The atom and ion dissipation takes place on the boundary: both the atoms and ions can diffuse away from the boundary, and at the same time, some atoms can become ionized, and then all the ions also drift under Coulomb forces [70]. To describe the loss of Ag atoms and ions from the narrow cylinder, both diffusion and drift are considered. Inside the CB tip, uniform distributions of atoms and ions are assumed. By applying Gauss's Law to the cylinder of CB tip, the electric field is obtained inside (including the boundary of) the cylinder.

$$E(r) = \frac{\rho r}{\varepsilon_0 \varepsilon_r} \tag{51}$$

where E(r) is the electric field at position r from the axis, ρ is the ion charge density, ε_0 is the vacuum permittivity and ε_r is the relative permittivity. Ions on the boundary drift at a velocity proportion to the magnitude of electric field, according to the equation below.

$$v(r) = \mu E(r) \tag{52}$$

where v(r) is the drift velocity, and μ is the mobility. The number of atom and ion dissipation equation within time dt is obtained below, where n_i is the ion density, n_a is the atom density, v_0 is the average diffusion velocity, also a negative sign is considered as the loss of atoms and ions (decrease of radius),

$$-(n_i + n_a)2\pi r \cdot dr = (n_i v(r) \cdot dt + (n_i + n_a)v_0 \cdot dt)2\pi r \tag{53}$$

Thus the radius dynamic equation is given below

$$\frac{dr}{dt} = -\frac{n_i v(r) + (n_i + n_a)v_0}{n_i + n_a} \tag{54}$$

For the fact that the number of atoms and ions is very small inside the CB tip, and the ionic processes of some atoms also take place, an approximation is made by assuming $n_i \gg n_a$. Also because the diffusion can happen in any direction and randomly, another assumption is that the drift velocity is much greater than the average diffusion velocity in our model. That is, $v(r) \gg v_0$. Thus the equation (54) can be simplified into

$$\frac{dr}{dt} = -v(r) = -\mu \frac{\rho r}{\varepsilon_0 \varepsilon_r} = -\frac{r}{\tau_r} \tag{55}$$

where τ_r is a new physical parameter and $\tau_r = \frac{\varepsilon_0 \varepsilon_r}{\mu \rho}$.

By integrating over time t, the following two expressions for the CB filament radius $r(\theta, t)$ and area $A_{tip}(t)$ at time t are obtained, respectively, where θ is the polar angle, A_0 is the initial CB filament area, and τ_r is the time constant for the change in filament radius.

$$r(\theta, t) = r(\theta) \exp\left(-\frac{t}{\tau_r}\right) \tag{56}$$

$$A_{tip}(t) = \int \frac{1}{2} r^2(\theta, t) d\theta = A_0 \exp\left(-\frac{2t}{\tau_r}\right) \tag{57}$$

The conductance G of the CB tip is given by

$$G = \frac{A_{tip}(t)\sigma}{h} = \frac{A_0 \sigma}{h} \exp\left(-\frac{2t}{\tau_r}\right) = G_0 \exp\left(-\frac{t}{\tau_g}\right) \tag{58}$$

where σ is the conductivity, and $\tau_g = \frac{\tau_r}{2}$ is the conductance decay time constant.

5.5.5 Model derivations: dynamic capacitance model

To extract parameters for model validation from a transient current test, we simulated the dynamic capacitance of our devices. A parasitic capacitance, and a time-varying CB tip capacitance are taken into account in this model. The capacitors in the circuit are influential in experimentally observing the conductance decay. The capacitors in the model consist of wire parasitic capacitance C_0, the CB tip gap region capacitance C_g, and the device dielectric material capacitor C_d. C_d and C_0 can be summed together in the simulation. As in **Figure 19** and **Figure 20**, C_g is the capacitance of CB gap region, which also includes capacitance beyond the CB end formed inside the dielectric material near the CB gap region. The gap region capacitance excludes the CB tip. The derived device capacitance is given by

$$C_g = C_t \exp(\frac{t}{\tau_c})$$

(59)

C_t is the initial dynamic capacitance in the gap region. The detailed derivation steps are in the follows.

$$C_g = \frac{\varepsilon A(t)}{d} = \frac{\varepsilon (A_{CB} - A_{tip}(t))}{d} = C_{CB} - C_{tip} \cdot \exp(-\frac{t}{\tau_g}) \approx C_{CB} - C_{tip} \cdot (1 - \frac{t}{\tau_g})$$

$$= (C_{CB} - C_{tip})(1 + \frac{C_{tip}}{(C_{CB} - C_{tip})} \frac{t}{\tau_g}) = C_t(1 + \frac{t}{\tau_c}) \approx C_t \exp(\frac{t}{\tau_c}),$$

(60)

$$where\ C_t \approx C_{CB} - C_{tip}$$

$$\tau_c = \frac{C_{CB} - C_{tip}}{C_{tip}} \tau_g > \tau_g$$

C_g is the net capacitance of CB gap region surrounding the tip, C_{tip} is the capacitance with area of CB tip, C_{CB} is the overall capacitance of the CB body end to the electrode (capacitance with area of CB body). The gap region capacitance should exclude the CB tip, and the corresponding area

equals the total CB body area subtracts the tip area. Thus the gap capacitance is calculated by subtracting the capacitance with tip area from the overall capacitance C_{CB} with area of CB body.

$$\frac{dr}{dt} < 0$$

$$r(t = t_0) = r_0, r(t = t_1) = r_1$$
$$t_0 < t_1, r_0 > r_1$$
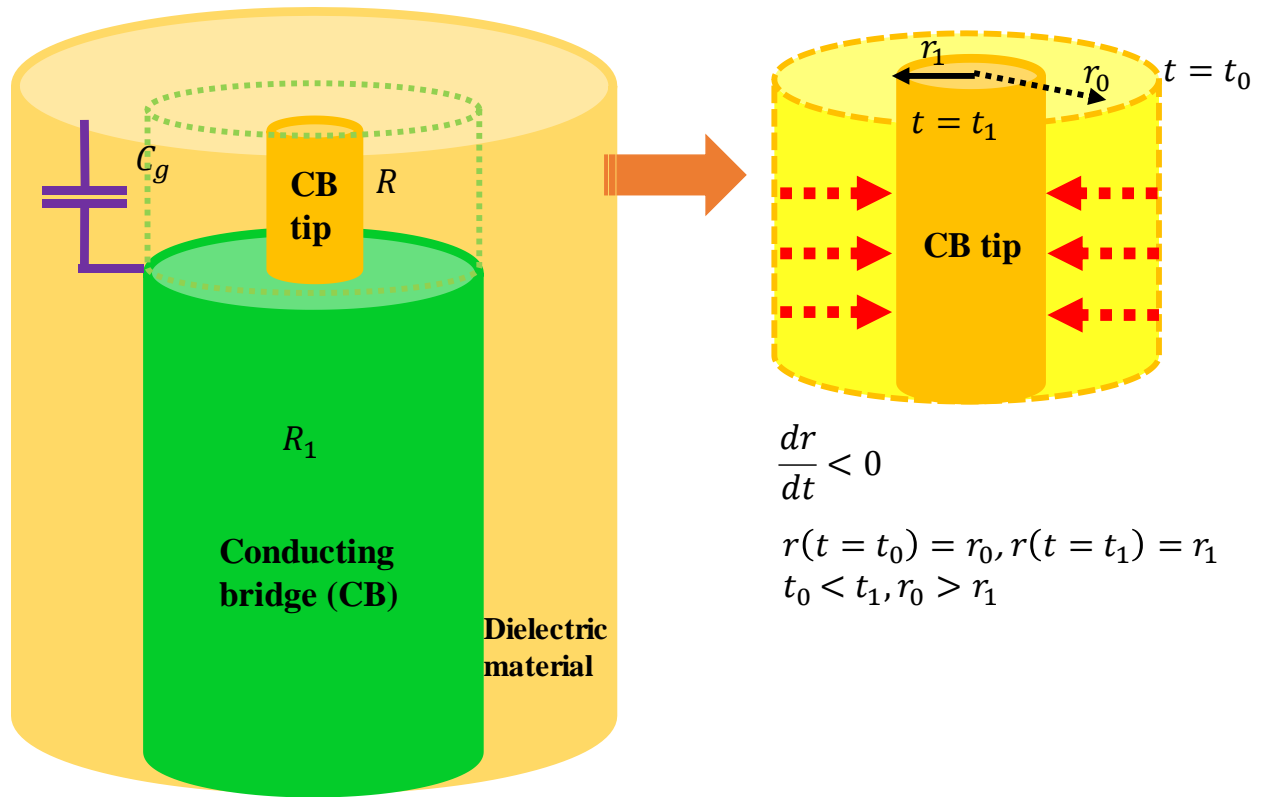
Figure 19. Dynamic capacitance model. The gap length can be viewed constant in the exponential decay model. The CB tip decreases while the gap capacitance increases. The area A(t) of the gap capacitor is the area without any atoms/ions (non-CB tip region), and increases a small amount, while the atoms/ions in the CB tip diffuse. The evolution of gap capacitance follows a slow increasing exponential function.

5.5.6 Initial state test and capacitance model verification

A dynamic transient test was performed to trace the decay of the device conductance. Different voltages were applied to turn a device ON and then turned off with different fall times so that the conductance decay could be observed. The fall times used in our setup were 1us and 10us, which were long enough to be comparable with the built-in circuit response time. The test setup included a significant capacitive current background and thus a circuit model was built to extract the capacitive current and verify the simulation accuracy. As shown in **Figure 20**, the CB body resistance was represented as R1, and CB tip resistance as R. The current flowed through the CB body resistance R1 first and then separated into two branches of both R **and** C_g.

R_0: wire resistance $\quad$ C_0: analyzer capacitance
R_1: CB body resistance $\quad$ C_g: CB tip region capacitance
R: CB tip varying resistance $\quad$ C_d: device dielectric material capacitance

current

peak

rise $\quad$ fall

Delay (V=0) $\quad$ read

In

R_0

C_0

C_d

R_1

R

C_g

Out

Parameter analyzer
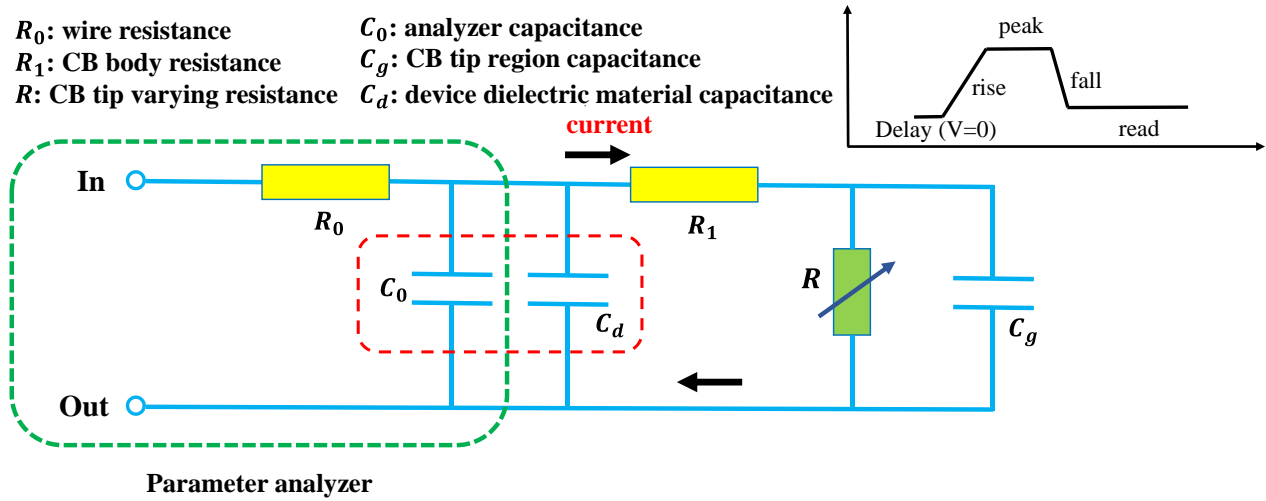
Figure 20. Circuit diagram for simulation and waveform. R1 is the CB body resistance excluding the CB tip, R is the CB tip resistance, Cd and Cg are dielectric and CB tip gap capacitors respectively. Current through device R1 is simulated. Also the currents through R and Cg are simulated and compared.

82

In the experiment, initially small voltages were tested on devices to trace the initial virgin states, so that the circuit model could be validated and compared with the decay after turning ON. In **Figure 21**, the simulation current curve is shown against experiment testing data @0.5V and @1.1V respectively. (More comparisons are listed in the supplementary data.) The simulation started from the first voltage pulse as in the experiment, and all device parameters were kept constant (capacitance C_g was fixed, and resistance R was in OFF state) for this low voltage virgin state test in our simulations. The simulation curves matched well with the experimental data in **Figure 21**. The delayed current caused by capacitance in the experimental setup was observed. Some current noise can be seen in the data. The noise was not considered in the simulation. The simulation curve accurately follows the median of the experimental data. The simulation current through the CB gap capacitor as a function of the current through the CB tip resistor is also shown. The results confirm that our circuit model and initial device resistance and capacitance parameters are correct. The above experiment was performed on a device which we called Device 1. For the following experiment another device of Device 2 on the same sample was tested. Both devices were of the same size.
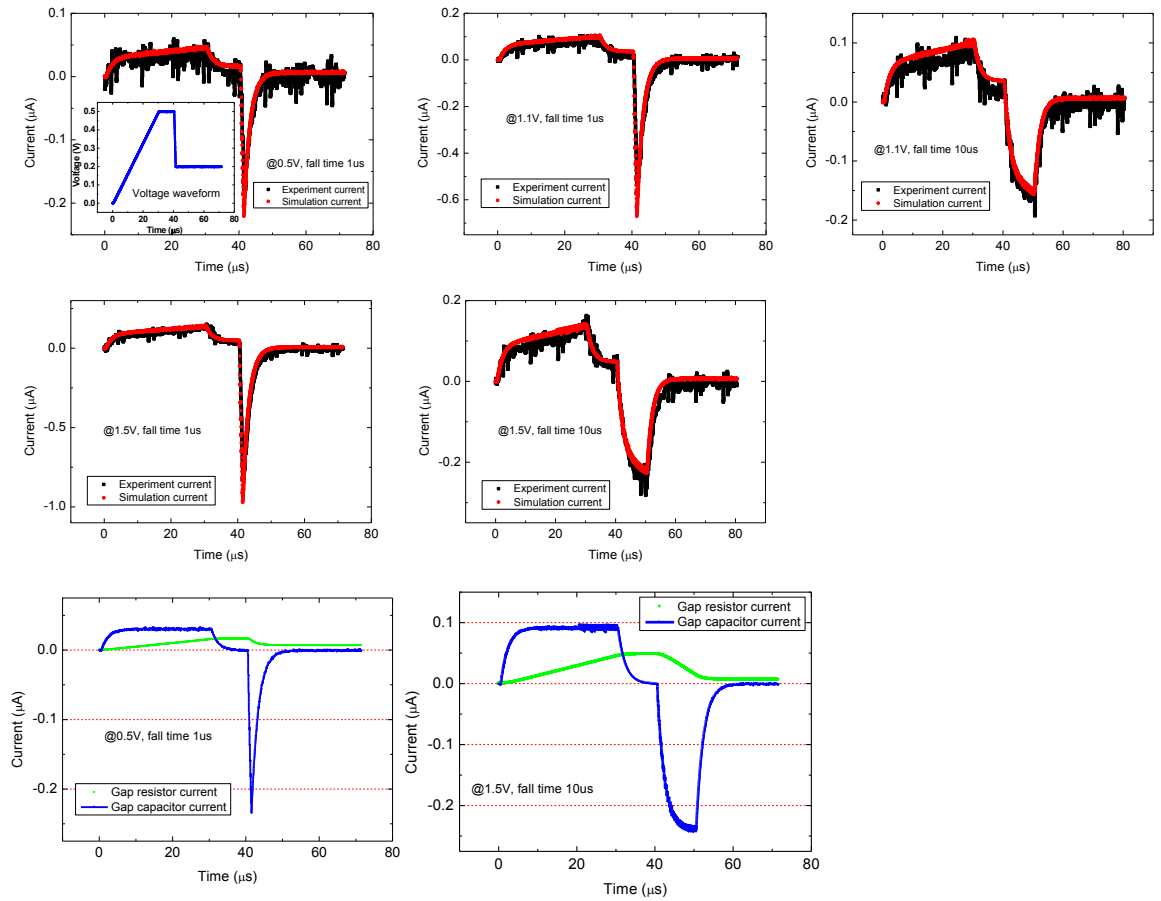
Figure 21. Initial state validation (Device 1). The device is tested under small voltages to verify the device capacitance and circuit diagram model. Two fall times are used in the experiment (1us and 10us). All simulated device parameters are kept constant in this initial state validation. All simulation current matches the experiment data well. The waveform of 0.5V is shown in the inset.

5.5.7   High voltage switching and decay model verification

After the initial virgin state tests, higher voltages were applied and data was collected for decay model validation. The results of 1.7V and 2.1V were shown in

Figure 22. The starting point of the waveform (at time t=0) corresponded to the ON state of the device, and starting from that, the test voltage decreased with a fall time of 1us or 10us respectively, until the voltage reached the value of the reading voltage of 0.2V, after which the test voltage remained constant.

For the decay simulations, at first the device conductance in its ON state was read from experiment data, and then the simulation voltage pulses were decreased according to the experimentally applied voltages. Also the holding voltage above which the CB filament and CB tip structures could be maintained should be taken into account. When the test voltage was still above the holding voltage (the simulation parameter was 1.5V), the device was still ON and no decay happened. Thus during that period the device was simulated in its ON state and all device parameters were those of the ON state. The CB tip resistance R and gap capacitance C_g were kept constant in their initial values. The ON state resistance value was still relatively high; details are given in the following section. When the voltage dropped below the holding voltage, the exponential evolution of both CB tip resistance R and gap capacitance C_g was simulated. When the dynamic resistance R reached the OFF state value threshold, the time evolution of both capacitance and resistance was stopped. Afterwards the current was simulated while keeping all these parameters fixed at OFF state values. All simulation curves fit the experimental data well. Simulated current through the gap resistor and capacitor are also shown in

85

Figure 22. And a turning point on the capacitor and resistor current curves was observed, which indicated the voltage had decreased below the holding voltage, and dynamic evolution of resistance and capacitance began. All simulation parameters are listed in **Table 5**.

Table 5. Simulation parameters.

Device	$C_0 + C_d$	C_t	R_0	R_1[a]	R[b]	τ_g	τ_c
Device 1		1.9 pF		1M Ω			
Device 2	2 pF	2.5 pF	8 Ω	1.3M Ω (Voltage <2.0V) 1.1M Ω (Voltage ≥2.0V))	30M Ω	5 μs	100 μs

[a]R_1 parameter in case of Device 3 is set for two different values for two range of voltages. Higher voltage (≥2.0V) makes stronger CB and higher LRS conductance, thus R_1 is set a lower value in this voltage range.
[b]R is the value of CB tip in its OFF state.
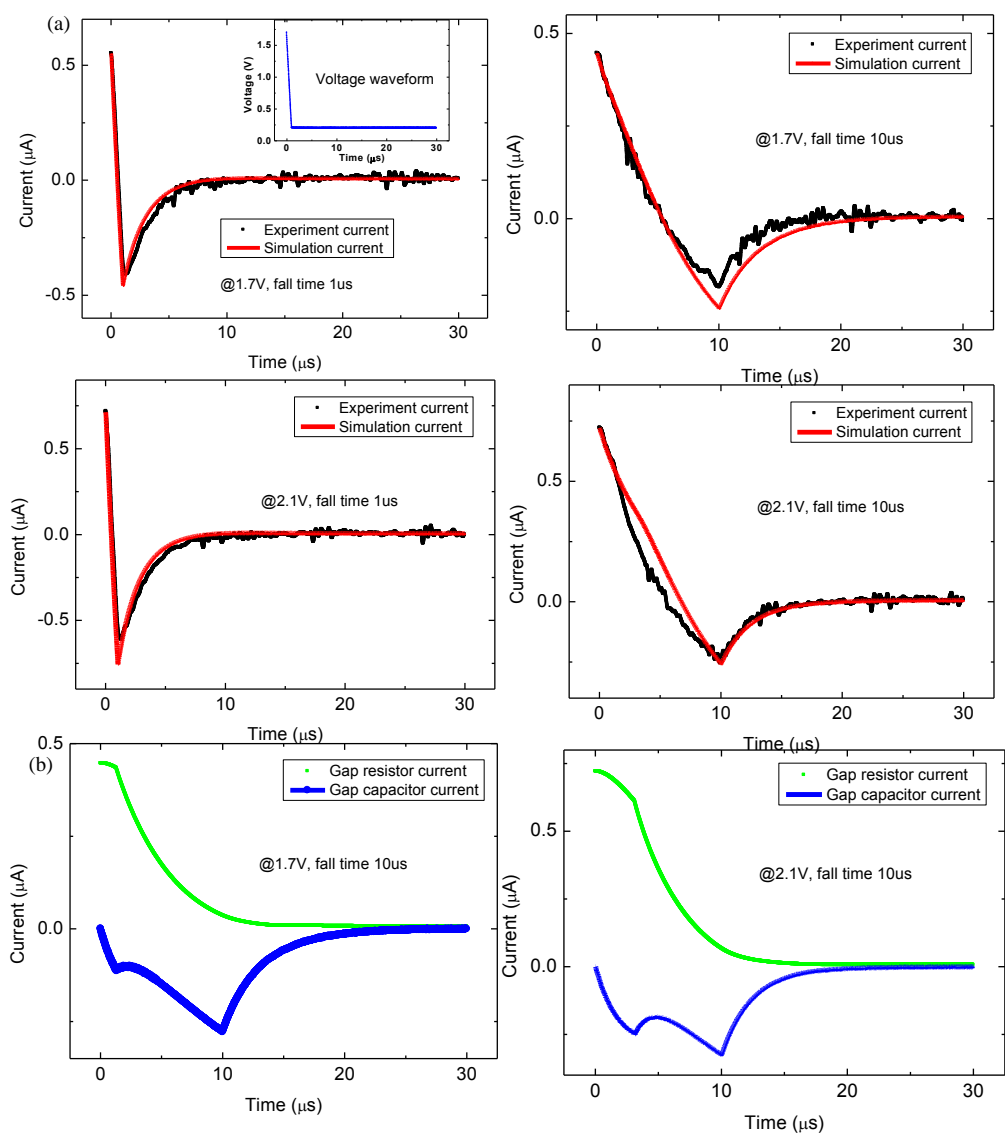
Figure 22. Decay model comparison and validation (Device 2). Another device is switched ON and afterwards the decay is traced by using two fall times (1us and 10us) to verify the correctness of CB tip decay model. Voltages in range of 1.7 ~ 2.1V are tested and simulated current matches the experiment data well. Simulated capacitor and gap resistor current are shown.

More simulation results of voltages are shown in **Figure 23**. The simulation results under test conditions 1.8V, 1.9V, and 2.0V are compared with the experiment data, for 1us and 10us fall time respectively. The simulation results are obtained using the same parameters in Table **5**. From the simulation result comparisons, only small errors occur in our model, which further validates the accuracy of our model against experiment data.
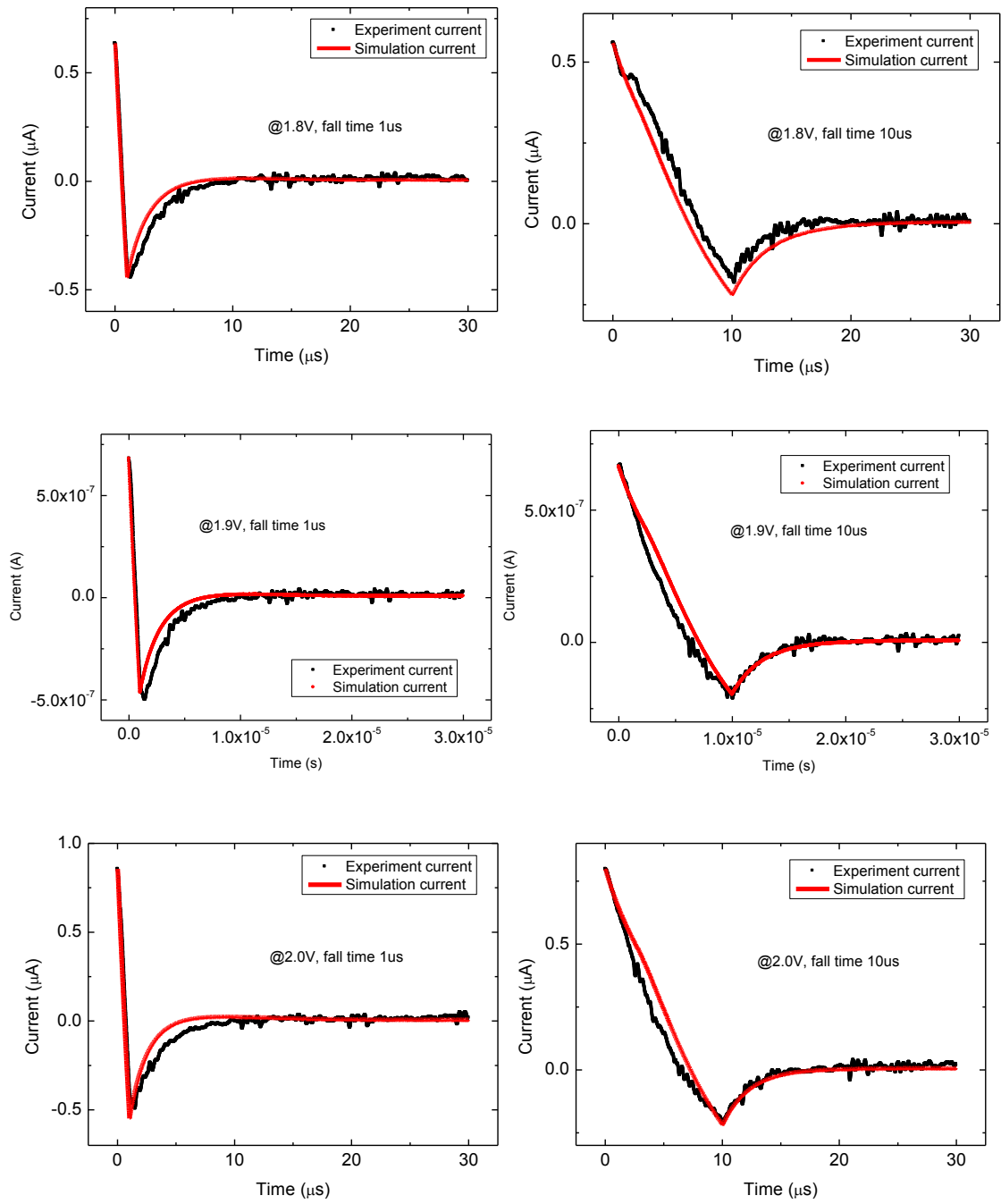
Figure 23. Simulation results of conductance/current decay at voltages of 1.8V, 1.9V, 2.0V. All simulation curves fit the experiment data well.

5.5.8 Experiment test to sweep the selector device to ON state (Device 1)

Initial sweep tests were performed on Device 1 to investigate the ON switching property. Small current jumps could be observed, which corresponded to conductance increasing caused by atomic motions inside the device. Different voltages were tested, from 0.1V up to 0.7V, with 0.1V as intervals. Dramatic current jumps were seen at about 0.5V. Details of the experiment curves are shown in **Figure 24**.
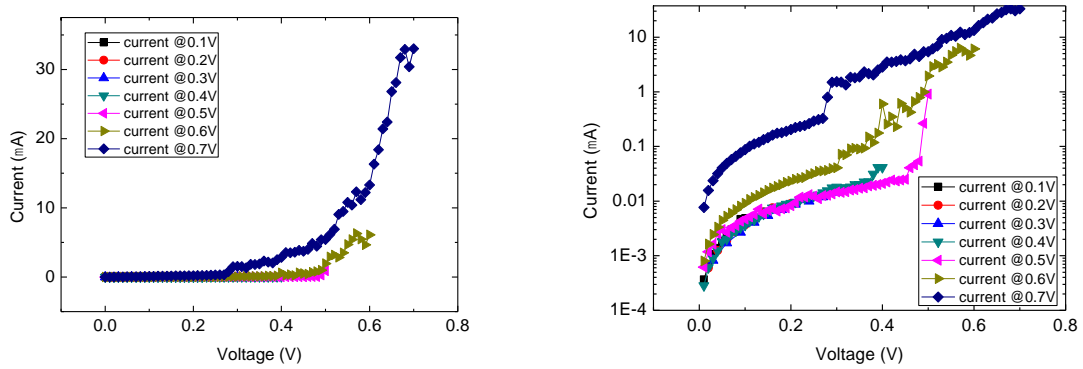

Figure 24. Voltage sweep from 0V to 0.1~0.7V to test the ON switching voltage (Device 1). Significant ON switching was observed at 0.5V. Linear and log plots are shown.

5.5.9 Experiment to sweep Device 1 to ON state with fixed voltage range

In addition, experiment was performed by applying 0V to 0.5V voltage ramping sweeps, to observe the device ON switching property. The device conductance showed multiple small increasing jumps in magnitude, in **Figure 25**. The conductance jump during ON switching is at most 0.15 quantum conductance. The conductance jump is caused by atoms moving on the surface or inside the CB body and tip region. That confirms the atomic motion causes conductance change to be less than one quantum conductance (0.15 as the largest jump).

As in **Figure 25**, the top two figures **Figure 25** (a)(b) show all the voltage sweep experiment results, with linear and log plots respectively. The plot **Figure 25** (c) in the middle in which the curve 17 and 18 show the typical switching curves of a device. The bottom two figures **Figure 25** (d)(e) show the calculated conductance increment, normalized by a quantum conductance. From the experiment data, we calculate the conductance first by dividing the experiment current by the experiment voltage, at each measurement time. In this way we can obtain a time series of conductance of the device, over multiple consecutive switching tests. After that we calculate the difference of conductance between two consecutive experiment time spots, and the result is shown in **Figure 25** (d). **Figure 25** (e) shows a boxplot of the conductance difference, which is a distribution of conductance difference. Those two plots **Figure 25** (d)(e) show that the maximum conductance jump is 0.15 quantum conductance.
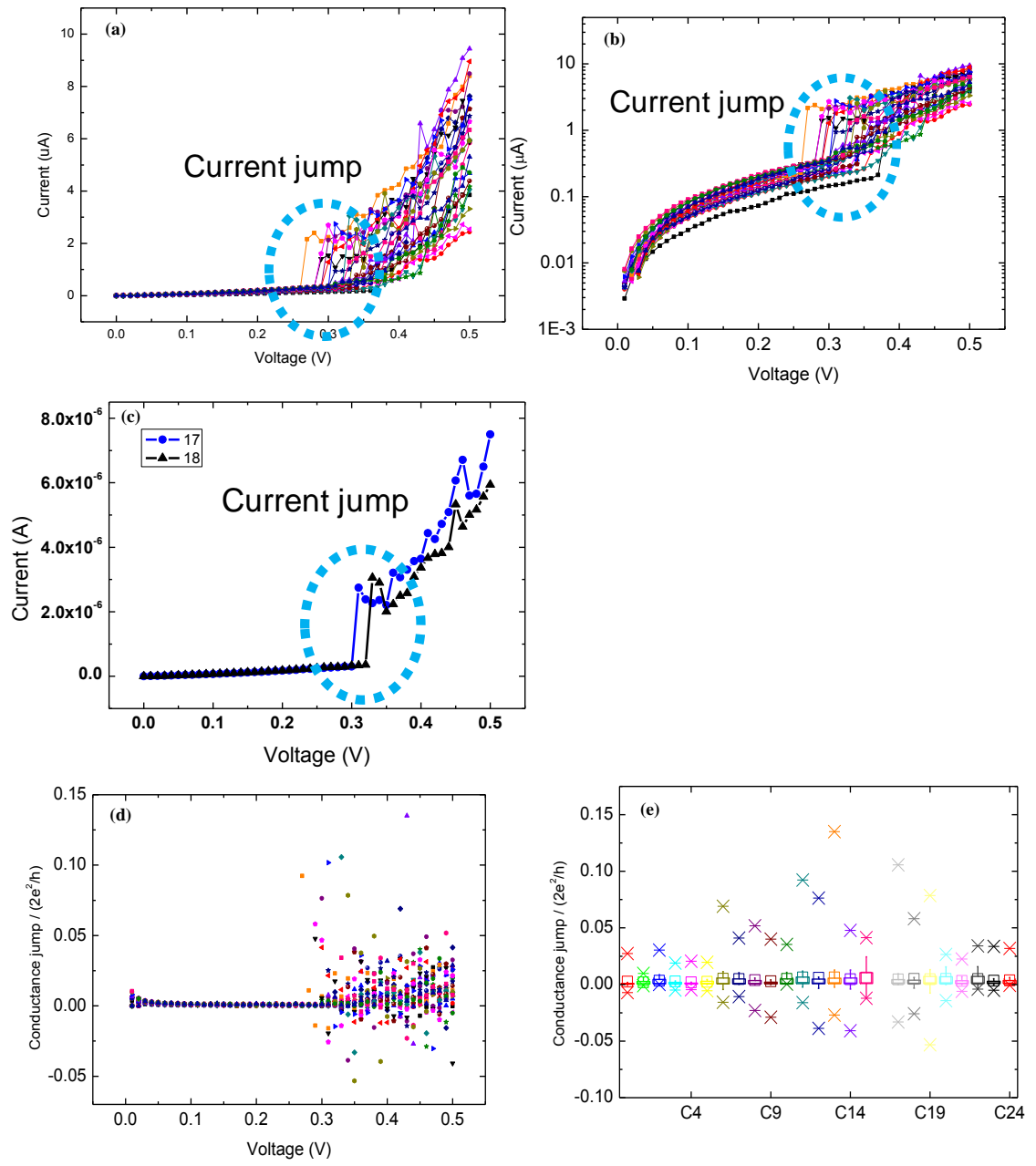
Figure 25. Current measurement @ 0.5V (Device 1). Volatile switching is repeatable at this voltage. Conductance jump is observed but is less than one quantum conductance. Maximum conductance jump during sweep is calculated to be 0.15 quantum conductance.

5.5.10 Explanation of high resistance in ON state

To explain why the ON state resistance value is high, the current was read and the resistance of the device in the ON state was calculated, as shown in **Figure 26**. The LRS (Low Resistance State) is above 2M Ohm, which is highly resistive. According to the formula for quantum conductance

$$G = \frac{2e^2}{h}T$$

(61)

where G is the conductance, and T is the tunneling transmission probability, we can infer that the device in the ON state contains tunneling barriers which electrons tunnel through with a probability far less than 1 (about 0.006). That can be explained by assuming the structure of the CB consists of discontinuous atom clusters as depicted in **Figure 18**, and energy barriers exist between those clusters.
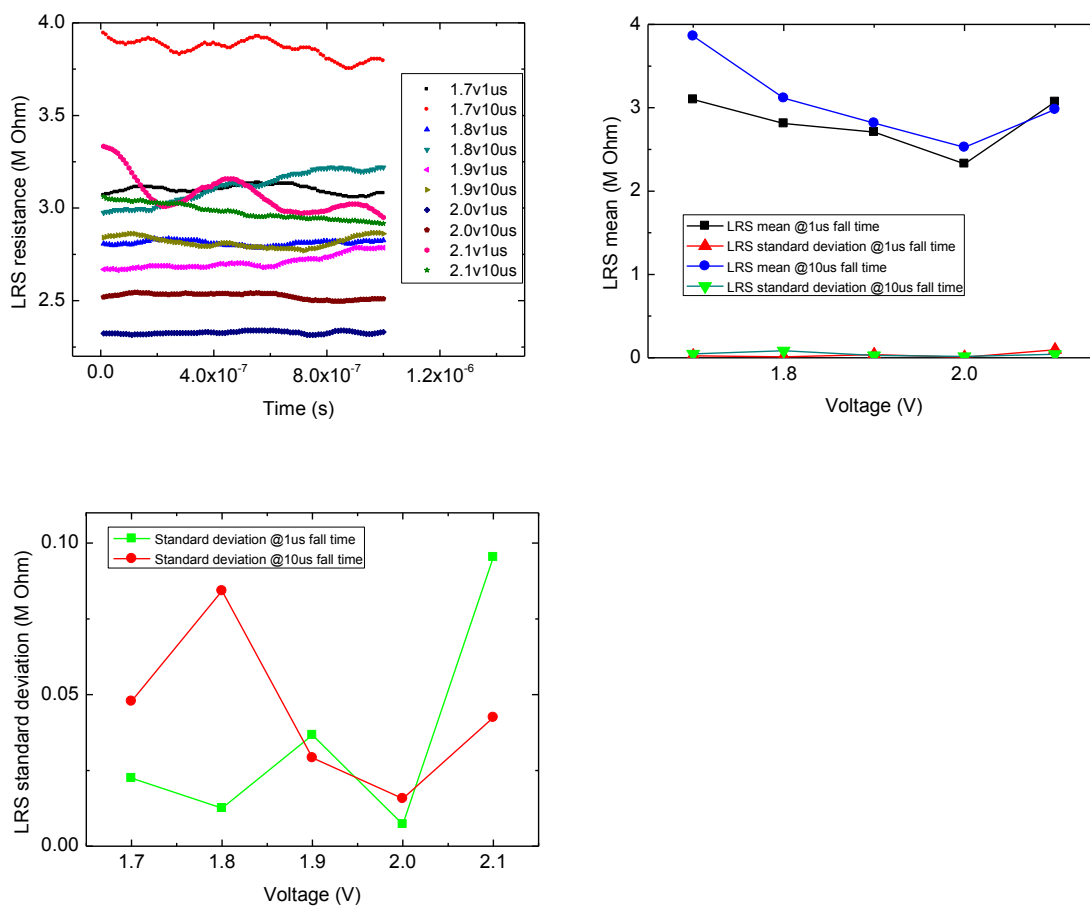
Figure 26. The data is from Device 2. LRS resistance is lower for higher voltage. Mean and standard deviation of LRS resistances are calculated from data directly. LRS resistance is above 2M Ohm and very resistive, which means Ag clusters may exist discontinuously in the CB structure.

5.5.11 Linear relation of decay time and device initial decay resistance LRS

The decay time is calculated from the equation of radius/ conductance, as in equation (58), starting from ON state value LRS, to OFF state value. In our model simulation, we record the total time for the device resistance decays from LRS to completely OFF. The relation shows an approximation of linear curve, as shown in **Figure 27**.

In **Figure 27**, the linear relation of decay time and initial LRS shows that the higher resistance of device initial state needs less time to dissipate the conducting bridge tip. The higher resistance means that the CB and/or CB tip is narrower than in lower resistance state. From our model, and as in **Figure 18** and **Figure 19**, the radius is smaller in higher resistance of device initial state, thus the total dissipation time of radius is less, and conductance decay time is less than that in lower resistance of device initial state.
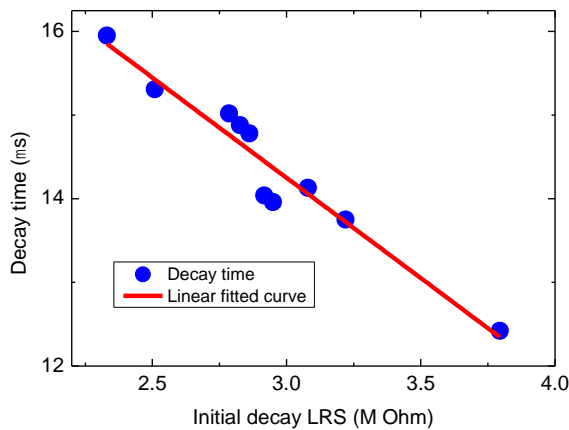

Figure 27. Linear dependence of decay time vs. initial LRS state resistance. The 10 initial decay LRS values are read at 1.7V up to 2.1V, with 1us and 10us fall times respectively and 0.1V as the voltage interval.

5.5.12 Device switching test at different temperatures (Device 3 & 4)

Low temperature measurements are performed to investigate the barrier height of oxide material. Switching is difficult in lower temperatures, and also difficult to control the CB size. Ions tend to be frozen in low temperatures, which means CB is more stable than in higher temperatures. In the experiment, we tested the virgin state by applying low voltages (0~0.5V/-0.5V), and measured the current. In this way we can obtain the nonlinear IV curve, from which we can extract the energy barrier. The experiment results including the IV and extracted barrier height U_a are shown in **Figure 28**. And in this experiment, the current compliance is removed.

Beside the virgin state test, we also measured the switching of such a selector device under low temperatures. In this test experiment, the current compliance is set to control the device and prevent it from becoming short by high current. Switching including both ON and OFF/decay under different temperatures are shown in **Figure 29** for Device 3 and **Figure 30** for Device 4.

For Device 3, as shown in **Figure 29**, in the temperature of 275K, 250K and 225K, the ON and OFF/decay switching can happen, according to the experiment results. For the ON switching, that shows the electric field provides enough energy for the atom/ion to change its configuration inside the CB, which causes the device to turn ON. For the OFF/decay, because the temperature is still relatively high, the atom and ion motion including the diffusion and drift can overcome the energy barrier, which causes the CB tip decay to occur. But in 200K, the switching does not happen. The possible explanations can be that, in low temperatures, the atoms and ions move very slowly, and the thermal fluctuations cannot afford the atom/ion to overcome the energy barrier. Thus the CB is relatively stable. To turn a device ON/OFF, higher voltages are required in low temperatures.

For Device 4, as shown in **Figure 30**, we can see ON switching and decay in temperature 200K, 100K and 90K, while no switching at all in temperature 175K, 150K and 125K. From this result, we can see that the atom and ion distribution can influence the local electric field, and also the randomness influence the device switching property. So while in some lower temperatures (100K and 90K) the device shows ON/OFF switching, the switching does not happen in relatively higher temperatures (175K, 150K, 125K). The switching of the device under temperature 100K and 90K can be explained by that the CB and CB tip configuration favor the atom and ion motions, and the surface energy and tension is easier for those atoms and ions to move and overcome the energy barrier, which causes the device to turn ON under electric field [83]. However, the switching in 100K is not very stable, and only a single switching curve is observed. That just proves that the "cold" atoms and ions move very slowly and almost frozen. The switching in 90K shows many large fluctuations, which also shows that the electric field controls the device switching and drives the atoms and ions to move very drastically, also in this case we can infer that the atoms and ions can move easier in this CB and CB tip configuration structure. In temperature 175K, 150K, 125K, no switching is observed, which shows the atoms and ions have less energy to move and change the configuration the conducting bridge inside the device, even under external electric field.
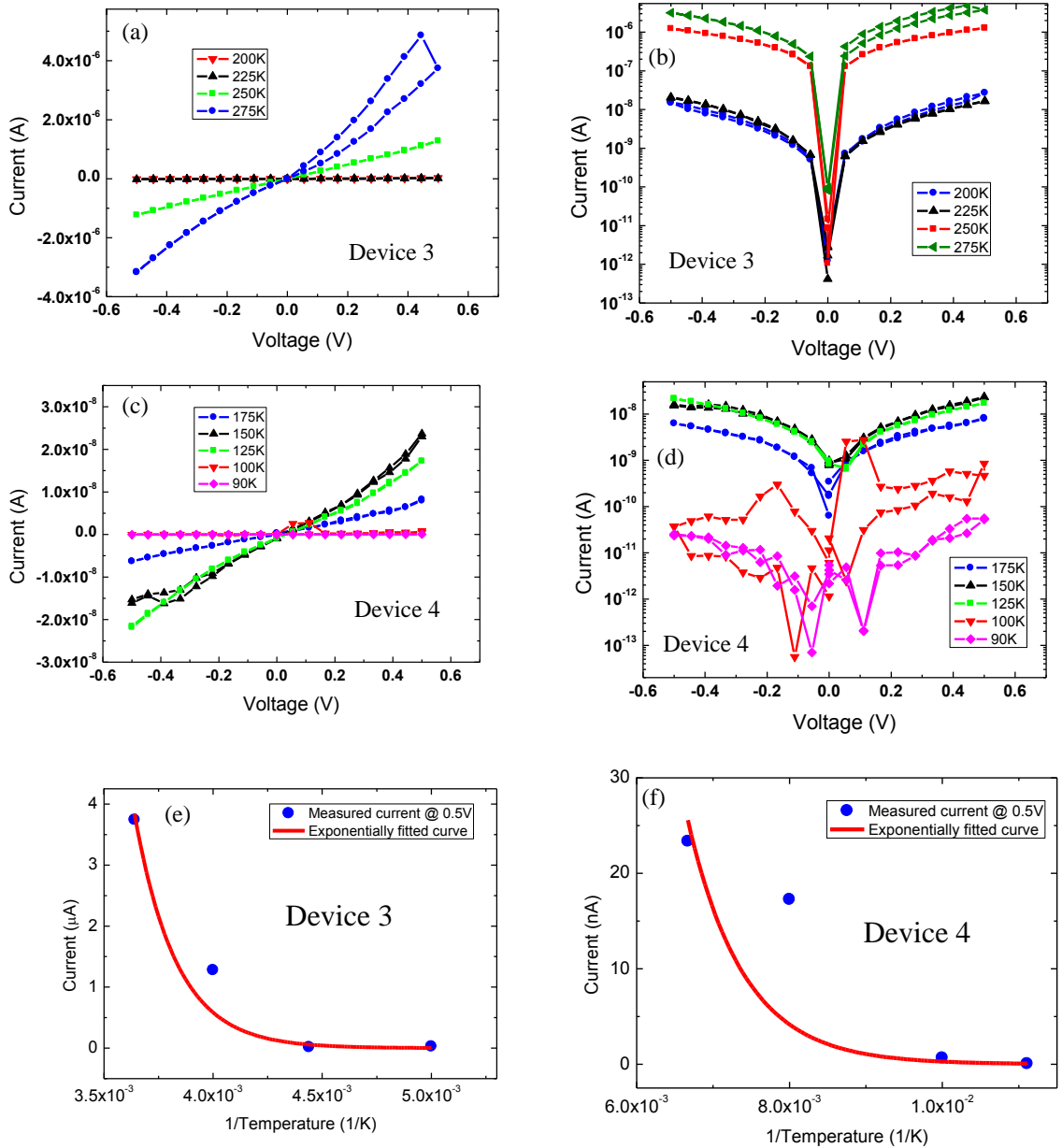
Figure 28. Initial resistance states measured at different temperatures, for the two devices respectively (Device 3 and 4). Both linear and log of the current are plotted, as in the insets (a)(b)(c)(d). Using equation $I \sim \exp(-\frac{U_a}{kT})$, we can obtain barrier height Ua=0.45eV device 3 in the inset (e); and for device 4, Ua= 0.12eV in the inset (f). Differences are observed in those approximated values of barrier height for different devices. Relatively large errors are observed in (c)(d), due to the noise in the low temperature measurement.
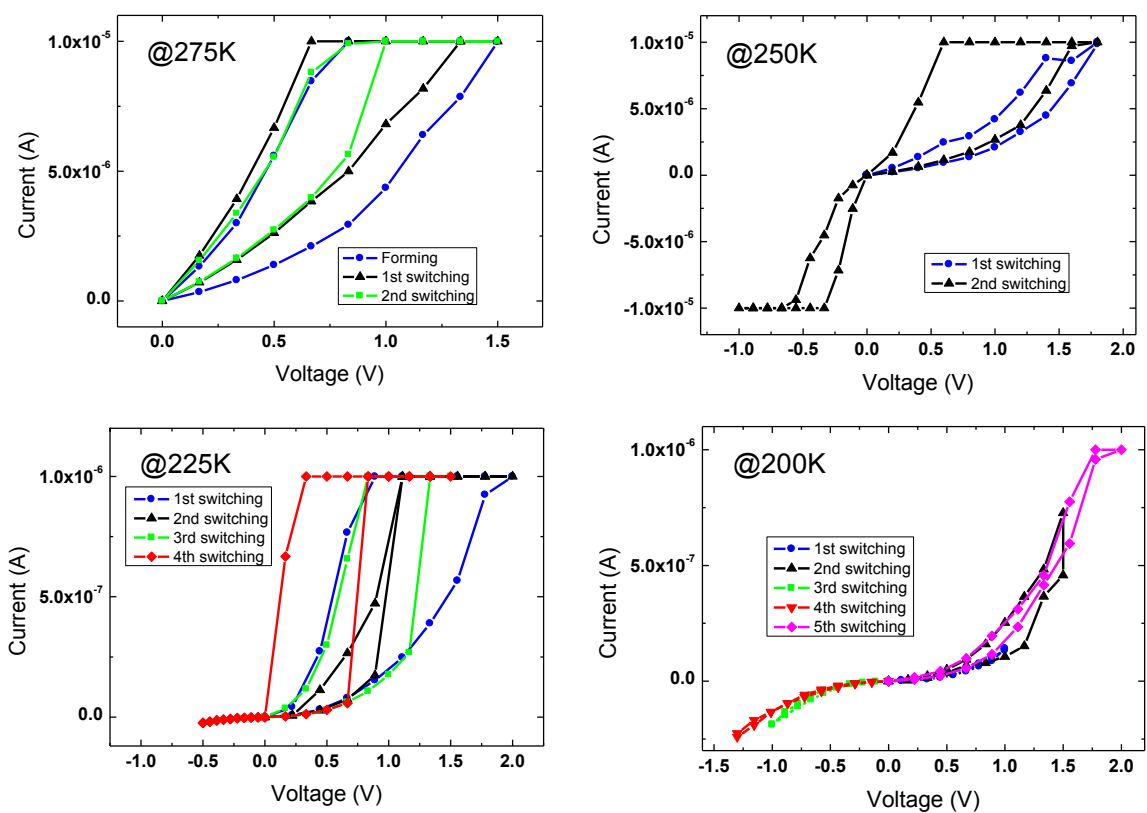
Figure 29. Switching experiment in low temperatures (Device 3). Multiple ON and OFF (decay) switching can happen in temperature 275K, 250K and 225K respectively, and no switching is observed in 200K.
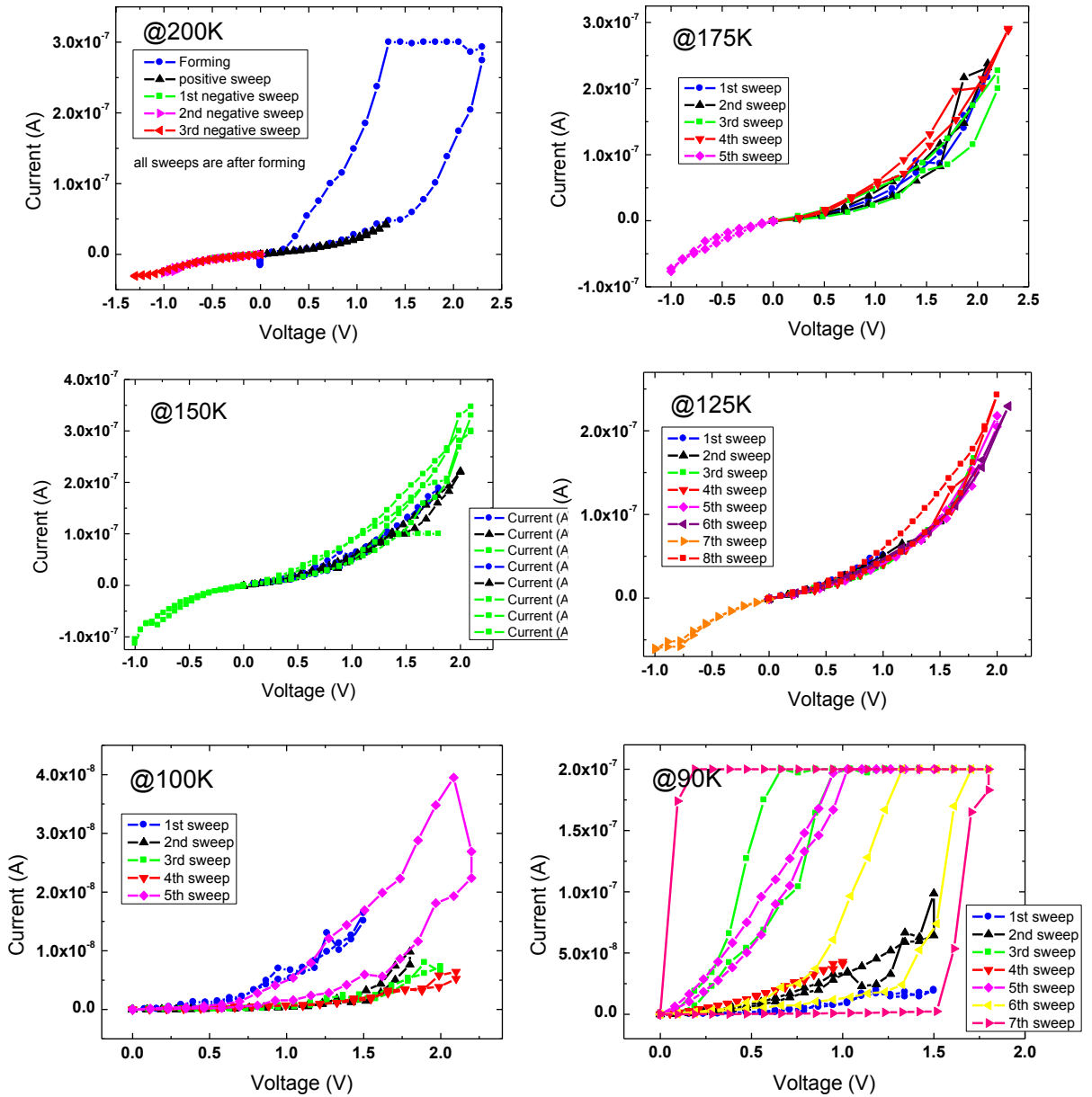
Figure 30. Switching experiment in low temperatures (Device 4). Multiple ON and OFF (decay) switching can happen in temperature 200K, 100K and 90K respectively, and no switching is observed in 175K, 150K and 125K. The switching is not stable in 100K and 90K.

5.6   SUMMARY

In this work, a model was proposed for the off-switching of a novel HfOx selector device. The model includes dynamic evolution of both resistance and capacitance. The background capacitive current due to the testing setup was accounted for, which enabled observation of the electrical conductance decay after reduction of the applied bias below a critical threshold. The modeling current curve matched the experimental data well over a wide voltage range, which confirmed the accuracy of our model.

6.0   CONCLUSION

The development requirement for fast computing speed, short memory accessing time, long storage retention time and endurance puts both memristors and selectors as the most promising candidates for future memory and computing technologies. The memristors have the advantages of non-volatility, high endurance, long retention and fast switching speed of nanoseconds, while the selectors have high nonlinearity and also the fast switching speed. Developing models of the memristors and selectors can be used to gain insight into why those devices have such promising properties, and understand how to better investigate and improve the devices for future applications. My research work on modeling both the memristors and selectors solves essential questions and problems in the understanding of those devices. In addition, my models can be directly used for circuit simulations, which can be used for future memory storage and computing applications.

To summarize, my research work mainly builds the following memristor and selector models, and solves the problems on how to apply the memristors and selectors to the storage applications and computing applications.

- Nonlinear switching memristor model: $TiO_2 - TiO_{2-x}$ memristor modeling.

$TiO_2 - TiO_{2-x}$ memristor is one of the most popular memristors in research. The typical $TiO_2 - TiO_{2-x}$ device shows a nonlinear switching curve, with time varying resistance values during the ON state of a device. My model is based on physical classic transport, and verified by experiment data, in both static IV curve and real time transient resistance data. The model proposes a region partition method which is novel, and which also solves the dynamics of the transition region, i.e the filament front. Starting from that, the model can be used to compute the ON and OFF switching times. Also an approximated analytical solution to the state variable which is the filament position (transition region position) of a memristor can be solved.

This model can be used to describe the nonlinear memristor dynamics and to compute the approximated switching times of a memristor.

- Linear switching memristor model: TaO_x memristor modeling.

TaO_x memristor is very promising in memory applications, due to its fast switching time, high endurance and large ON/OFF ratio. TaO_x memristor is linear because the ON state is a constant resistance value, and from the IV curve, it is a straight line after turning ON. My research work on modeling TaO_x memristor focuses on solving the two state variables, based on nonlinear transport physics and thermal effects. In this model, thermophoresis is included for the filament area variable dynamics. The filament gap width variable dynamics is based on the nonlinear transport. Both variables are dependent on the temperature. And the temperature is calculated in this model. Also the temperature induced conductivity change is considered in the model.

This two state variable memristor model is verified by both pulse sweep test, and state test. In addition, the dynamics of the two state variables and temperature is simulated. Those physical parameters can show the underlying mechanisms which are related to the device switching properties.

This model is further integrated into a Verilog-A model and can be used in circuit simulations.

- Selector based on volatile conducting bridges: HfO_x selector modeling.

HfO_x selector device is a high nonlinearity device with fast switching speed. The switching mechanism is based on the volatile conducting bridge, which is formed inside the device by electric field and ion motions, and which can dissipate if external voltage is below the holding voltage. The model solves a decay equation for both conducting bridge tip resistance and gap capacitance. Diffusion and drift are both considered in the model derivations. The model is verified first by the virgin state test, which confirms the correctness and accuracy of our capacitance model. Then the decay model is verified by test data which different fall times of voltages and experiment data of conductance decay, for a range of testing voltages.

The HfO_x selector model explains quantitatively how the decay happen in the HfO_x selector, and proposes two dynamic equations for conductance and capacitance decay. The model can be applied with memristor model for memory simulations and predictions.

BIBLIOGRAPHY

[1] L. Chua, "Memristor-the missing circuit element," *IEEE Transactions on Circuit Theory,* vol. 18, no. 5, pp. 507-519, Sep. 1971.

[2] L. Chua, S.M. Kang, "Memristive Devices and Systems," *Proceedings of the IEEE,* vol. 64, no. 2, pp. 209-223, Feb. 1976.

[3] J.J. Yang, M.D. Pickett, X. Li, D.A.A. Ohlberg, D.R. Stewart, R.S. Williams, "Memristive switching mechanism for metal/oxide/metal nanodevices," Nature nanotechnology, vol. 3, no. 429, July 2008.

[4] D. B. Strukov, G. S. Snider, D. R. Stewart, and R. S. Williams, "The missing memristor found," Nature, vol. 453, no. 7191, p. 80–83, May. 2008.

[5] Yang, J.J., Miao, F., Pickett, M.D., Ohlberg, D.A.A., Stewart, D.R., Lau, C.N., Williams, R. S, "The mechanism of electroforming of metal oxide memristive switches," *Nanotechnology,* vol. 20, p. 215201, May 2009.

[6] D. B. Strukov and R. Stanley Williams, "Exponential ionic drift: fast switching and low volatility of thin-film memristors," Applied Physics A, vol. 94, no. 3, pp. 515-519, Mar 2009.

[7] R. Waser, R. Dittmann, G. Staikov, and K. Szot, "Redox-Based Resistive Switching Memories − Nanoionic Mechanisms, Prospects, and Challenges," *Advanced Materials,* vol. 21, no. 25-26, p. 2632–2663, Jul 2009.

[8] D. Ielmini, "Modeling the Universal Set/Reset Characteristics of Bipolar RRAM by Field- and Temperature-Driven Filament Growth," *Electron Devices, IEEE Transactions on ,* vol. 58, no. 12, pp. 4309 - 4317, Dec 2011.

[9] D. B. Strukov, J. L. Borghetti, and R. S. Williams, "Coupled ionic and electronic transport model of thin-film semiconductor memristive behavior," *Small,* vol. 5(9), p. 1058–1063, 2009.

[10] Yu, S., Guan, X. & Wong, H. S. P. , "Conduction mechanism of TiN/HfOx/Pt resistive switching memory: A trap-assisted-tunneling model," Appl. Phys. Lett, no. 99, 2011.

[11] J. J. Yang, Borghetti, J., Murphy, D., Stewart, D. R., & Williams, R. S., "A family of electronically reconfigurable nanodevices," *Advanced Materials,* vol. 21, no. 37, pp. 3754-3758, 2009.

[12] D. S. Jeong, H. Schroeder, and R. Waser, "Coexistence of bipolar and unipolar resistive switching behaviors in a Pt/TiO2/Pt stack," *Electrochemical and Solid State Letters,* vol. 10, pp. G51-G53, 2007.

[13] Strukov, D. B., Alibart, F., & Williams, R. S., "Thermophoresis/diffusion as a plausible mechanism for unipolar resistive switching in metal–oxide–metal memristors," *Applied Physics A,,* vol. 107, no. 3, pp. 509-518, 2012.

[14] L. O. Chua, "Device Modeling via basic nonlinear circuit elements," *IEEE Trans.Circuits Syst. CAS-27,* pp. 1014-1044, 1980.

[15] R. S. Williams and M. D. Pickett, "The Art and Science of Constructing a Memristor Model," in *Memristors and Memristive Systems*, New York, Springer, 2014, pp. 93-104.

[16] J. J. Yang, F. Miao, M. D. Pickett, D. A. A. Ohlberg, D. R. Stewart, C. N. Lau and R. S. Williams, "The mechanism of electroforming of metal oxide memristive switches," *Nanotechnology,* vol. 20, no. 215201, May 2009.

[17] L Zhang, Z Chen, JJ Yang, B Wysocki, N McDonald, Y Chen, "A compact modeling of TiO2-TiO2–x memristor," *Applied Physics Letters,* vol. 102, no. 15, p. 153503, Apr 2013.

[18] M. D. Pickett, D. B. Strukov, J. L. Borghetti, J. J. Yang, G. S. Snider, D. R. Stewart and R. S. Williams, "Switching dynamics in titanium dioxide memristive devices," *Journal of Applied Physics,* vol. 106, no. 7, p. 074508, Oct 2009.

[19] Nardi, F., Larentis, S., Balatti, S., Gilmer, D. C., & Ielmini, D, "Resistive switching by voltage-driven ion migration in bipolar RRAM—Part I: Experimental study," *IEEE Transactions on,* vol. 59, no. 9, pp. 2461-2467, 2012.

[20] Larentis, S., Nardi, F., Balatti, S., Gilmer, D. C., & Ielmini, D, "Resistive switching by voltage-driven ion migration in bipolar RRAM—Part II: Modeling," *IEEE Transactions on,* vol. 59, no. 9, pp. 2468-2475, 2012.

[21] Lee, M. J., Lee, C. B., Lee, D., Lee, S. R., Chang, M., Hur, J. H., Kim, Y., Kim, C., H. Seo, D., Seo, S., Chung, U., Yoo, I., & Kim, K., "A fast, high-endurance and scalable non-volatile memory device made from asymmetric Ta2O5−x/TaO2−x bilayer structures," *Nature materials,* vol. 10, pp. 625-630, 2011.

[22] Park, G. S., Kim, Y. B., Park, S. Y., Li, X. S., Heo, S., Lee, M. J., Chang, M., Kwon, J. H., Kim, M., Chung, U., Dittmann, R., Waser, R. & Kim, K., "In situ observation of filamentary conducting channels in an asymmetric Ta2O5− x/TaO2− x bilayer structure," *Nature communications,* vol. 4, 2013.

[23] Wei, Z., Kanzawa, Y., Arita, K., Katoh, Y., Kawai, K., Muraoka, S., Mitani, S., Fujii, S., Katayama, K., Iijima, M., Mikawa, T., Ninomiya, T., Miyanaga, R., Kawashima, Y., Tsuji, K., Himeno, A., Okada, T., Azuma, R., Shimakawa, K., Sugaya, H., Takagi, T., Yasuhara, R., Horiba, K., Kumigashira, H., & Oshima, M, "Highly reliable TaOx ReRAM and direct evidence of redox reaction mechanism," Electron Devices Meeting, 2008. IEDM 2008. IEEE International, pp. 1 - 4, Dec 2008.

[24] J.J. Yang, J.P. Strachan, F. Miao, M.X. Zhang, M.D. Pickett, W. Yi, D.A-A Ohlberg, G. Medeiros-Ribeiro, R. S. Williams, "Metal/TiO2 interfaces for memristive switches," *Appl Phys A ,* vol. 102, p. 785–789, Mar 2011.

[25] Yang, J. J., Strukov, D. B. & Stewart, D. R., "Memristive devices for computing," *Nature nanotechnology,* vol. 8, pp. 13-24, 2013.

[26] J. J. Yang, M.-X. Zhang, J. P. Strachan, F. Miao, M. D. Pickett, R. D. Kelley, G. Medeiros-Ribeiro and R. S. Williams, "High switching endurance in TaOx memristive devices," *Applied Physics Letters,* vol. 97, no. 23, pp. 232102 - 232102-3, Dec 2010.

[27] D. H. Kwon, K. M. Kim, J. H. Jang, J. M. Jeon, M. H. Lee, G. H. Kim, et al, "Atomic structure of conducting nanofilaments in TiO2 resistive switching memory," *Nature Nanotechnology,* vol. 5, pp. 148-153, Feb 2010.

[28] F. Miao, W. Yi, I. Goldfarb, J. Joshua Yang, M.-X. Zhang, M. D. Pickett, J. Paul Strachan, G. Medeiros Ribeiro, and R. Stanley Williams, "Continuous electrical tuning of the chemical composition of TaO(x)-based memristors," ACS Nano, vol. 6, no. 3, p. 2312–2318, 2012.

[29] F. Miao, J. Paul Strachan, J. Joshua Yang, M.-X. Zhang, I. Goldfarb, A. C. Torrezan, P. Eschbach, R. D.Kelley, G. Medeiros-Ribeiro, and R. S. Williams, "Anatomy of a Nanoscale Conduction Channel Reveals the Mechanism of a High-Performance Memristor," *Adv. Mater.,* vol. 23, no. 47, p. 5633, 2011.

[30] Strachan, J. P., Pickett, M. D., Yang, J. J., Aloni, S., David Kilcoyne, A. L., Medeiros‐Ribeiro, G., and Williams, R. S., "Direct identification of the conducting channels in a functioning memristive device," *Advanced Materials,* vol. 22, no. 32, pp. 3573-3577, 2010.

[31] Y. Zhang, N. Deng, H. Wu, Z. Yu, J. Zhang, and H. Qian, "Metallic to hopping conduction transition in Ta2O5−x/TaOy resistive switching device," Applied Physics Letters, vol. 105, p. 063508, 2014.

[32] F. Miao, J. J. Yang, J. P. Strachan, D. Stewart, R. S. Williams, and C. N. Lau, "Force modulation of tunnel gaps in metal oxide memristive nanoswitches," *Applied Physics Letters,* vol. 95, p. 113503, Sep 2009.

[33] R. Münstermann, J. J. Yang, J. P. Strachan, G. Medeiros-Ribeiro, R. Dittmann, and R. Waser, "Morphological and electrical changes in TiO2 memristive devices induced by

electroforming and switching," *physica status solidi (RRL) – Rapid Research Letters,* vol. 4, pp. 16-18, 2010.

[34] S. Menzel, M. Waters, A. Marchewka, U. Böttger, R. Dittmann, and R. Waser, "Origin of the Ultra-Ultranonlinear Switching Kinetics in Oxide-Based Resistive Switches," *Advanced Functional Materials,* vol. 21, p. 4487–4492, 2011.

[35] Strachan, J. P., Torrezan, A. C., Miao, F., Pickett, M. D., Yang, J. J., Yi, W., Medeiros-Ribeiro, G., & Williams, R. S., "State Dynamics and Modeling of Tantalum Oxide Memristors," Electron Devices, IEEE Transactions on, vol. 60, no. 7, pp. 2194-2202, 2013.

[36] Mickel, P. R., Lohn, A. J., Choi, B. J., Yang, J. J., Zhang, M. X., Marinella, M. J., James, C. D., & Williams, R. S, "A physical model of switching dynamics in tantalum oxide memristive devices," *Applied Physics Letters,* vol. 102, no. 22, p. 223502, 2013.

[37] Kim, S., Kim, S. J., Kim, K. M., Lee, S. R., Chang, M., Cho, E., Kim, Y. B., Kim, C. J., Chung, U. & Yoo, I. K., "Physical electrothermal thermal model of resistive switching in bi-layered resistance-change memory," *Scientific Reports,* no. 3, 2013.

[38] S. Yu, X. Guan, and H. S. P. Wong, "Conduction mechanism of TiN/HfOx/Pt resistive switching memory: A trap-assisted-tunneling model," Appl. Phys. Lett., vol. 99, no. 6, 2011.

[39] D. Ielmini, F. Nardi, and S. Balatti, "Evidence for Voltage-Driven Set/Reset Processes in Bipolar Switching RRAM," *IEEE Trans. Electron Devices,* vol. 59, no. 8, p. 2049–2056, Jun 2012.

[40] J. Frenkel, "On Pre-Breakdown Phenomena in Insulators and Electronic Semi-Conductors," Physical Review, vol. 54, no. 8, p. 647, Oct 1938.

[41] G. Medeiros-Ribeiro, F. Perner, R. Carter, H. Abdalla, M. D. Pickett and R. S. Williams, "Lognormal Switching Times for Titanium Dioxide Bipolar Memristors: Origin and Resolution," *Nanotechnology 22, 095702,* 2011.

[42] Kwon, D.H., Kim, K.M., Jang, J.H., Jeon, J.M., Lee, M.H., Kim, G.H., Li, X.S., Park, G.S., Lee, B., Han, S. and Kim, M., 2010. Atomic structure of conducting nanofilaments in TiO2 resistive switching memory. Nature nanotechnology, 5(2), pp.148-153.

[43] Park, S.G., Magyari-Kope, B. and Nishi, Y., 2011. Impact of Oxygen Vacancy Ordering on the Formation of a Conductive Filament in for Resistive Switching Memory. IEEE Electron Device Letters, 32(2), pp.197-199.

[44] Wang, W., Fujita, S., & Wong, S. S. (2009). RESET mechanism of TiOx resistance-change memory device. IEEE Electron Device Letters, 30(7), 733-735.

[45] Jeong, H. Y., Lee, J. Y., & Choi, S. Y. (2010). Interface-Engineered Amorphous TiO2-Based Resistive Memory Devices. Advanced Functional Materials, 20(22), 3912-3917.

[46] Cagli, C., Nardi, F., & Ielmini, D. (2009). Modeling of set/reset operations in NiO-based resistive-switching memory devices. IEEE Transactions on Electron Devices, 56(8), 1712-1720.

[47] Russo, U., Ielmini, D., Cagli, C., & Lacaita, A. L. (2009). Filament conduction and reset mechanism in NiO-based resistive-switching memory (RRAM) devices. IEEE Transactions on Electron Devices, 56(2), 186-192.

[48] Larentis, S., Nardi, F., Balatti, S., Gilmer, D. C., & Ielmini, D. (2012). Resistive switching by voltage-driven ion migration in bipolar RRAM—Part II: Modeling. IEEE Transactions on Electron Devices, 59(9), 2468-2475.

[49] Bersuker, G., Gilmer, D. C., Veksler, D., Yum, J., Park, H., Lian, S., ... & Shluger, A. (2010, December). Metal oxide RRAM switching mechanism based on conductive filament microscopic properties. In 2010 IEEE International Electron Devices Meeting, IEDM 2010.

[50] Long, S., Cagli, C., Ielmini, D., Liu, M., & Suñé, J. (2012). Analysis and modeling of resistive switching statistics. Journal of Applied Physics, 111(7), 074508.

[51] Bersuker, G., Gilmer, D.C., Veksler, D., Kirsch, P., Vandelli, L., Padovani, A., Larcher, L., McKenna, K., Shluger, A., Iglesias, V. and Porti, M., 2011. Metal oxide resistive memory switching mechanism based on conductive filament properties. Journal of Applied Physics, 110(12), p.124518.

[52] Jeong, H. Y., Lee, J. Y., & Choi, S. Y. (2010). Direct observation of microscopic change induced by oxygen vacancy drift in amorphous TiO2 thin films.

[53] Kamiya, K., Yang, M. Y., Park, S. G., Magyari-Köpe, B., Nishi, Y., Niwa, M., & Shiraishi, K. (2012). ON-OFF switching mechanism of resistive–random–access–memories based on the formation and disruption of oxygen vacancy conducting channels. Applied Physics Letters, 100(7), 073502.

[54] Kim, S. K., Kim, K. M., Jeong, D. S., Jeon, W., Yoon, K. J., & Hwang, C. S. (2013). Titanium dioxide thin films for next-generation memory devices. Journal of Materials Research, 28(03), 313-325.

[55] Gao, B., Sun, B., Zhang, H., Liu, L., Liu, X., Han, R., ... & Yu, B. (2009). Unified physical model of bipolar oxide-based resistive switching memory. IEEE Electron Device Letters, 30(12), 1326-1328.

[56] Makarov, A., Sverdlov, V., & Selberherr, S. (2011). Stochastic model of the resistive switching mechanism in bipolar resistive random access memory: Monte Carlo simulations. Journal of Vacuum Science & Technology B, 29(1), 01AD03.

[57] Li, D., Li, M., Zahid, F., Wang, J., & Guo, H. (2012). Oxygen vacancy filament formation in TiO2: A kinetic Monte Carlo study. Journal of Applied Physics, 112(7), 073512.

[58] Savel'ev, S. E., Alexandrov, A. S., Bratkovsky, A. M., & Williams, R. S. (2011). Molecular dynamics simulations of oxide memristors: Crystal field effects. Applied Physics Letters, 99(5), 053108.

[59] Savel'Ev, S. E., Alexandrov, A. S., Bratkovsky, A. M., & Williams, R. S. (2011). Molecular dynamics simulations of oxide memory resistors (memristors). Nanotechnology, 22(25), 254011.

[60] J. D. Jackson, Classical Electrodynamics, 3rd ed. (Wiley, New York, 1998).

[61] Burr, G. W., Virwani, K., Shenoy, R. S., Padilla, A., BrightSky, M., Joseph, E. A., ... & Bowers, A. N. (2012, June). Large-scale (512kbit) integration of multilayer-ready access-devices based on mixed-ionic-electronic-conduction (MIEC) at 100% yield. In VLSI Technology (VLSIT), 2012 Symposium on (pp. 41-42). IEEE.

[62] Choi, B. J., Zhang, J., Norris, K., Gibson, G., Kim, K. M., Jackson, W., ... & Williams, R. S. (2016). Trilayer tunnel selectors for memristor memory cells.Advanced Materials, 28(2), 356-362.

[63] Cuenot, S., Frétigny, C., Demoustier-Champagne, S., & Nysten, B. (2004). Surface tension effect on the mechanical properties of nanomaterials measured by atomic force microscopy. Physical Review B, 69(16), 165410.

[64] Gibson, G.A., Musunuru, S., Zhang, J., Vandenberghe, K., Lee, J., Hsieh, C.C., Jackson, W., Jeon, Y., Henze, D., Li, Z. and Williams, R.S., 2016. An accurate locally active memristor model for S-type negative differential resistance in NbOx. Applied Physics Letters, 108(2), p.023505.

[65] Jo, S. H., Kumar, T., Narayanan, S., Lu, W. D., & Nazarian, H. (2014, December). 3D-stackable crossbar resistive memory based on field assisted superlinear threshold (FAST) selector. In 2014 IEEE International Electron Devices Meeting (pp. 6-7). IEEE.

[66] Kim, S., Liu, X., Park, J., Jung, S., Lee, W., Woo, J., ... & Lee, D. (2012, June). Ultrathin (< 10nm) Nb 2 O 5/NbO 2 hybrid memory with both memory and selector characteristics for high density 3D vertically stackable RRAM applications. In VLSI Technology (VLSIT), 2012 Symposium on (pp. 155-156). IEEE.

[67] Kim, W. G., Lee, H. M., Kim, B. Y., Jung, K. H., Seong, T. G., Kim, S., ... & Kim, S. G. (2014). NbO 2-based low power and cost effective 1S1R switching for high density cross point ReRAM Application. In 2014 Symposium on VLSI Technology (VLSI-Technology): Digest of Technical Papers.

[68] Kund, M., Beitel, G., Pinnow, C.U., Rohr, T., Schumann, J., Symanczyk, R., Ufert, K.D. and Muller, G., 2005, December. Conductive bridging RAM (CBRAM): An emerging non-volatile memory technology scalable to sub 20nm. In IEEE International Electron Devices Meeting, 2005. IEDM Technical Digest.

[69] Lee, W., Park, J., Shin, J., Woo, J., Kim, S., Choi, G., Jung, S., Park, S., Lee, D., Cha, E. and Lee, H.D., 2012, June. Varistor-type bidirectional switch (J MAX> 10 7 A/cm 2, selectivity~ 10 4) for 3D bipolar resistive memory arrays. In VLSI Technology (VLSIT), 2012 Symposium on (pp. 37-38). IEEE.

[70] McBrayer, J. D., Swanson, R. M., & Sigmon, T. W. (1986). Diffusion of metals in silicon dioxide. Journal of The Electrochemical Society, 133(6), 1242-1246.

[71] Son, M., Lee, J., Park, J., Shin, J., Choi, G., Jung, S., Lee, W., Kim, S., Park, S. and Hwang, H., 2011. Excellent selector characteristics of nanoscale for high-density bipolar ReRAM applications. IEEE Electron Device Letters,32(11), pp.1579-1581.

[72] Srinivasan, V.S.S., Chopra, S., Karkare, P., Bafna, P., Lashkare, S., Kumbhare, P., Kim, Y., Srinivasan, S., Kuppurao, S., Lodha, S. and Ganguly, U., 2012. Punchthrough-diode-based bipolar RRAM selector by Si epitaxy. IEEE Electron Device Letters, 33(10), pp.1396-1398.

[73] Wang, M., Lian, X., Pan, Y., Zeng, J., Wang, C., Liu, E., Wang, B., Yang, J.J., Miao, F. and Xing, D., 2015. A selector device based on graphene–oxide heterostructures for memristor crossbar applications. Applied Physics A,120(2), pp.403-407.

[74] Waser, R. and Aono, M., 2007. Nanoionics-based resistive switching memories. Nature materials, 6(11), pp.833-840.

[75] Zhang, L., Redolfi, A., Adelmann, C., Clima, S., Radu, I.P., Chen, Y.Y., Wouters, D.J., Groeseneken, G., Jurczak, M. and Govoreanu, B., 2014. Ultrathin metal/amorphous-silicon/metal diode for bipolar RRAM selector applications. IEEE Electron Device Letters, 35(2), pp.199-201.

[76] Jo, S. H., Kumar, T., Narayanan, S., & Nazarian, H. (2015). Cross-point resistive RAM based on field-assisted superlinear threshold selector. IEEE Transactions on Electron Devices, 62(11), 3477-3481.

[77] Jo, S. H., Kumar, T., Narayanan, S., Lu, W. D., & Nazarian, H. (2014, December). 3D-stackable crossbar resistive memory based on field assisted superlinear threshold (FAST) selector. In 2014 IEEE International Electron Devices Meeting (pp. 6-7). IEEE.

[78] Ge, N., Zhang, M. X., Zhang, L., Yang, J. J., Li, Z., & Williams, R. S. (2014). Electrode-material dependent switching in TaO_x memristors. Semiconductor Science and Technology, 29(10), 104003.

[79] Kim, K. H., Gaba, S., Wheeler, D., Cruz-Albrecht, J. M., Hussain, T., Srinivasa, N., & Lu, W. (2011). A functional hybrid memristor crossbar-array/CMOS system for data storage and neuromorphic applications. Nano letters, 12(1), 389-395.

[80] Zhang, L., Ge, N., Yang, J. J., Li, Z., Williams, R. S., & Chen, Y. (2015). Low voltage two-state-variable memristor model of vacancy-drift resistive switches. Applied Physics A, 119(1), 1-9.

[81] Linn, E., Rosezin, R., Kügeler, C., & Waser, R. (2010). Complementary resistive switches for passive nanocrossbar memories. Nature materials,9(5), 403-406.

[82] Wedig, A., Luebben, M., Cho, D.Y., Moors, M., Skaja, K., Rana, V., Hasegawa, T., Adepalli, K.K., Yildiz, B., Waser, R. and Valov, I., 2016. Nanoscale cation motion in TaOx, HfOx and TiOx memristive systems.Nature nanotechnology, 11(1), pp.67-74.

[83] Brillo, J., & Egry, I. (2005). Surface tension of nickel, copper, iron and their binary alloys. Journal of materials science, 40(9-10), 2213-2216.

[84] Lee, H.Y., Chen, P.S., Wu, T.Y., Chen, Y.S., Wang, C.C., Tzeng, P.J., Lin, C.H., Chen, F., Lien, C.H. and Tsai, M.J., 2008, December. Low power and high speed bipolar switching with a thin reactive Ti buffer layer in robust HfO2 based RRAM. In 2008 IEEE International Electron Devices Meeting (pp. 1-4). IEEE.

[85] Gao, B., Yu, S., Xu, N., Liu, L.F., Sun, B., Liu, X.Y., Han, R.Q., Kang, J.F., Yu, B. and Wang, Y.Y., 2008, December. Oxide-based RRAM switching mechanism: A new ion-transport-recombination model. In 2008 IEEE International Electron Devices Meeting (pp. 1-4). IEEE.

[86] Yoshida, C., Tsunoda, K., Noshiro, H., & Sugiyama, Y. (2007). High speed resistive switching in Pt/TiO2/TiN film for nonvolatile memory application. Applied Physics Letters, 91(22), 3510.

[87] Borghetti, J., Snider, G. S., Kuekes, P. J., Yang, J. J., Stewart, D. R., & Williams, R. S. (2010). 'Memristive' switches enable 'stateful' logic operations via material implication. Nature, 464(7290), 873-876.

[88] Lee, M.J., Lee, C.B., Lee, D., Lee, S.R., Chang, M., Hur, J.H., Kim, Y.B., Kim, C.J., Seo, D.H., Seo, S. and Chung, U.I., 2011. A fast, high-endurance and scalable non-volatile memory device made from asymmetric Ta2O5− x/TaO2− x bilayer structures. Nature materials, 10(8), pp.625-630.

[89] Borghetti, J., Li, Z., Straznicky, J., Li, X., Ohlberg, D.A., Wu, W., Stewart, D.R. and Williams, R.S., 2009. A hybrid nanomemristor/transistor logic circuit capable of self-programming. Proceedings of the National Academy of Sciences, 106(6), pp.1699-1703.

[90] Kim, Y.B., Lee, S.R., Lee, D., Lee, C.B., Chang, M., Hur, J.H., Lee, M.J., Park, G.S., Kim, C.J., Chung, U.I. and Yoo, I.K., 2011, June. Bi-layered RRAM with unlimited endurance and extremely uniform switching. In VLSI Technology (VLSIT), 2011 Symposium on (pp. 52-53). IEEE.

[91] Chen, H. Y., Yu, S., Gao, B., Huang, P., Kang, J., & Wong, H. S. P. (2012, December). HfOx based vertical resistive random access memory for cost-effective 3D cross-point architecture without cell selector. In Electron Devices Meeting (IEDM), 2012 IEEE International (pp. 20-7). IEEE.

[92] Williams, R. S. (2008). How we found the missing memristor. IEEE spectrum,45(12), 28-35.

[93] Xia, Q., Robinett, W., Cumbie, M.W., Banerjee, N., Cardinali, T.J., Yang, J.J., Wu, W., Li, X., Tong, W.M., Strukov, D.B. and Snider, G.S., 2009. Memristor− CMOS hybrid integrated circuits for reconfigurable logic. Nano letters, 9(10), pp.3640-3645.

[94] Torrezan, A. C., Strachan, J. P., Medeiros-Ribeiro, G., & Williams, R. S. (2011). Sub-nanosecond switching of a tantalum oxide memristor.Nanotechnology, 22(48), 485203.

[95] Yang, J. J., Borghetti, J., Murphy, D., Stewart, D. R., & Williams, R. S. (2009). A family of electronically reconfigurable nanodevices. Advanced Materials,21(37), 3754-3758.

[96] Miao, F., Strachan, J.P., Yang, J.J., Zhang, M.X., Goldfarb, I., Torrezan, A.C., Eschbach, P., Kelley, R.D., Medeiros-Ribeiro, G. and Williams, R.S., 2011. Anatomy of a Nanoscale Conduction Channel Reveals the Mechanism of a High-Performance Memristor. Advanced materials, 23(47), pp.5633-5640.

[97] Snider, G., Kuekes, P., Hogg, T., & Williams, R. S. (2005). Nanoelectronic architectures. Applied Physics A, 80(6), 1183-1195.

[98] Strachan, J. P., Strukov, D. B., Borghetti, J., Yang, J. J., Medeiros-Ribeiro, G., & Williams, R. S. (2011). The switching location of a bipolar memristor: chemical, thermal and structural mapping. Nanotechnology, 22(25), 254015.

[99] Yang, J.J., Strachan, J.P., Xia, Q., Ohlberg, D.A., Kuekes, P.J., Kelley, R.D., Stickle, W.F., Stewart, D.R., Medeiros-Ribeiro, G. and Williams, R.S., 2010. Diffusion of adhesion layer metals controls nanoscale memristive switching.Advanced materials, 22(36), pp.4034-4038.

[100] Yu, S., & Wong, H. S. P. (2011). Compact modeling of conducting-bridge random-access memory (CBRAM). IEEE Transactions on Electron devices,58(5), 1352-1360.